CHALMERS

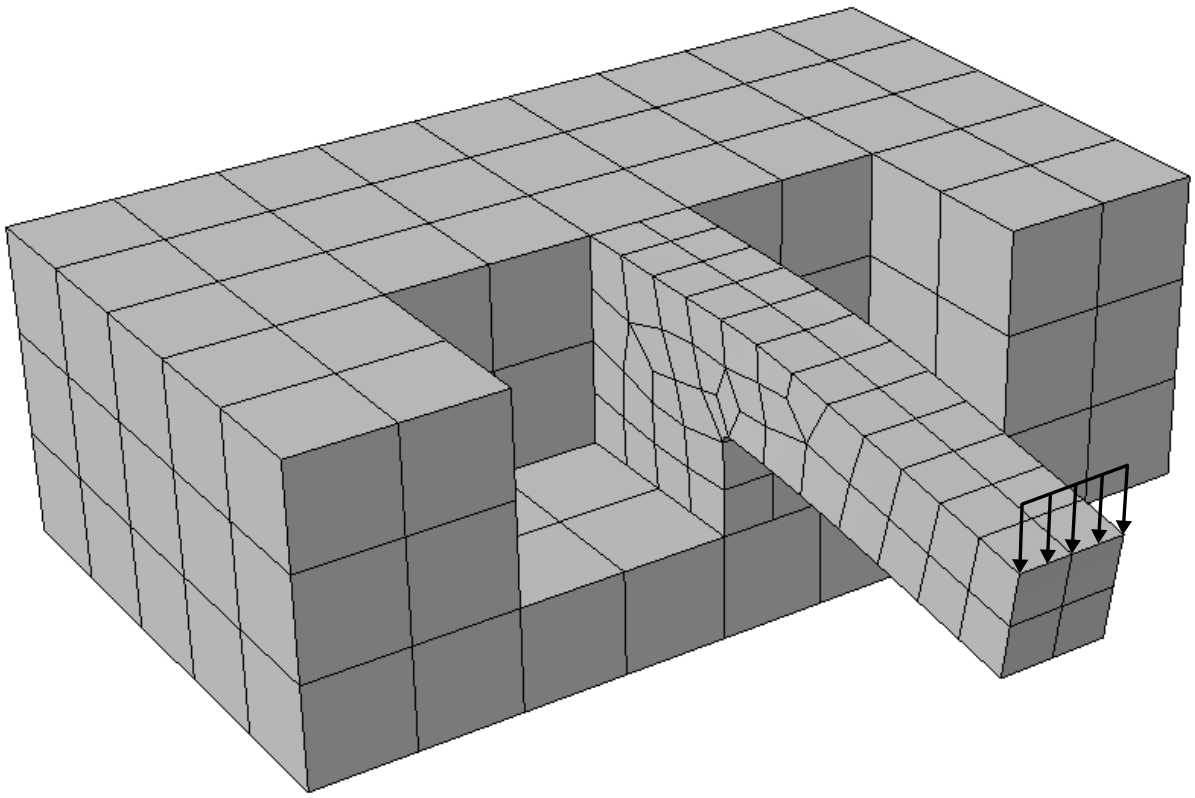

Finite Element Simulations of Microbeam Bending Experiments

Master's thesis in Applied Mechanics

JOHN WIKSTRÖM

Department of Applied Mechanics
CHALMERS UNIVERSITY OF TECHNOLOGY
Göteborg, Sweden 2017

MASTER'S THESIS IN APPLIED MECHANICS

Finite Element Simulations of Microbeam Bending Experiments

JOHN WIKSTRÖM

Department of Applied Mechanics
Division of Material & Computational Mechanics
CHALMERS UNIVERSITY OF TECHNOLOGY

Göteborg, Sweden 2017

Finite Element Simulations of Microbeam Bending Experiments

JOHN WIKSTRÖM

Master's thesis 2017:42
ISSN 1652-8557
Department of Applied Mechanics
Division of Material & Computational Mechanics
Chalmers University of Technology
SE-412 96 Göteborg
Sweden
Telephone: +46 (0)31-772 1000

Cover: Displacement plot from a microbeam bending simulation.

Chalmers Reproservice
Göteborg, Sweden 2017

Finite Element Simulations of Microbeam Bending Experiments

Master's thesis in Applied Mechanics
JOHN WIKSTRÖM
Department of Applied Mechanics
Division of Material & Computational Mechanics
Chalmers University of Technology

Abstract

The microstructure of metals is built up by grains. Each grain in turn has an anisotropic crystal structure with an individual crystal orientation. The mechanical behavior of single crystals can be modeled using so called crystal plasticity models. These crystal plasticity models are typically used as constitutive models in finite element analyses.

Multiscale modeling strategies may be used to link the micromechanical crystal behavior to the behavior of metals on the macroscale. In practice, it is the macroscale response that is of importance when assessing the performance of engineering components in the industry. However, for a multiscale analysis to be successful, we require an accurate crystal plasticity model for the metal of interest. It is today possible to perform experiments on the microscale with structures made from single crystals. Data from these experiments may then be used to calibrate a crystal plasticity model. Calibration here refers to the process of fitting a simulation response to the experimental data by finding the best values for the material parameters in the constitutive model.

The main objective of this thesis is to investigate the possibilities to use data from microbeam bending experiments in order to calibrate a specific crystal plasticity model. The microbeam bending experiments can be described as cantilever beam experiments in which each of the beams are subjected to a displacement controlled point load. During the experiments, photos are taken in order to evaluate force-deflection data for the contact point. The experiments were prepared and conducted by Anand Harihara Subramonia Iyer at the Department of Physics at Chalmers. Three microbeams were prepared in total for the experiments. Each of the microbeams was milled out from a single crystal of the superalloy Allvac 718 Plus. The three microbeams had different geometry and crystal orientation. One of the experiments was successful while the other two experiments unfortunately failed.

The first step in the project was to develop a finite element model in Abaqus which can be used to simulate microbeam bending experiments. An Abaqus Python script was written to set up the microbeam model. This script was written in a parametrized manner such that the user can specify the individual beam geometry, material parameters and important analysis settings. In order to use the specific crystal plasticity model as constitutive model in the Abaqus simulations, the microbeam model features a user-defined material model (UMAT). The UMAT was implemented by Magnus Ekh at the Department of Industrial and Materials Science at Chalmers.

The next step was to set up an optimization routine which can be used to calibrate the material parameters of the crystal plasticity model based on experimental data. This was achieved by coupling optimization code in Matlab with Abaqus simulations. The Nelder-Mead method, also called the simplex method, was chosen as optimization algorithm for this purpose.

Since limited data was acquired in the experiments, a calibration was first performed based on "experiment data" produced by three different microbeam finite element models. These microbeam models all had the same geometry but different crystal orientation. The data was produced with a known set of material parameter values which were then disturbed and "calibrated". In the case of a well-formulated optimization problem, the material parameter values used to produce the data are hopefully found in the calibration. The problem of calibrating the elastic parameters resulted in a non-unique solution. It was concluded that more response information is needed from the experiments (and the simulations) in order to uniquely find all the elastic parameters, force-deflection data is not enough. Calibration of the plastic responses were performed taking a limited set of the plastic material parameters into consideration. This decision was taken in order to promote a unique solution. It was judged that calibration of the omitted parameters would require more advanced response data, e.g. data for different load rates. Overall, the fictitious calibration resulted in well fitted force-deflection response curves. It was also concluded that the sensitivity for some plastic material parameters were higher than for other ones.

A calibration based on data from the real microbeam bending experiment was then performed. It was possible to obtain a well fitted force-deflection response through a calibration process. However, due to the

non-unique solution for the elastic parameters, two constraints that can be considered arbitrary were used. Also, the experimental data showed an overly stiff linear elastic response compared to the finite element simulation when using material parameters for the similar superalloy Inconel 718. This is probably due to inaccurate experimental data. In conclusion, the calibrated material parameters for Allvac 718 Plus resulted in a good response fit but is unlikely representative for the material.

In relation to the calibration, comparisons between the slip lines obtained in the experiments and the slip variables in the simulations were performed. These comparisons involved images from all experiments, including the ones that failed. However, no major conclusions could be made from these comparisons.

Keywords: crystal plasticity, microbeam bending, material model calibration

Preface

First of all I would like to thank my supervisor and examiner Magnus Ekh for his great support and help throughout the project. His invaluable knowledge and experience in constitutive modeling kept me on track and saved me trouble at several stages the last five months. I would also like to thank Magnus Colliander and Anand Harihara Subramonia Iyer for giving me an insight into their world of microscale experiments with metals. I hope that my thesis work in some way can contribute to your future research on crystal plasticity.

John Wikström
Göteborg, June 2017

Contents

1 Introduction

1.1 Background & Motivation

Superalloys is a class of alloys where its members show excellent mechanical properties in multiple regards. The combination of high mechanical strength at high temperatures accompanied with excellent corrosion and oxidation resistance makes superalloys suitable for some of the most extreme engineering applications. Within the group of superalloys, the nickel-based ones tend to stand out with extraordinary good properties. Nickel-based superalloys have gained extra traction within the aerospace and aircraft industry where they are commonly used in gas turbine engines. However, the properties of nickel-based superalloys are utilized in other applications as well, e.g. marine ships, nuclear reactors and defense industry applications [1].

The macroscale mechanical properties of a metal are strongly dependent on its microstructural composition which in turn depends on the constituents and the manufacturing process. Regarding modeling of the microscale of metals, various crystal plasticity models have been developed over the years and implemented as constitutive models in finite element analyses. If an accurate material model is available for the microscale, it can be used in a multiscale modeling strategy to numerically link the macroscale properties to those of the microscale, see Figure 1.1. Experiments on the microscale could thereby play a key role in any multiscale modeling strategy. In particular, data from such experiments can be used to calibrate crystal plasticity models.

In order to gain further knowledge of the microscale mechanical behavior of superalloys, microbeam bending experiments have recently been initiated at the Department of Physics, Chalmers. These experiments feature microbeams with lengths of 10 to 20 µm which each are milled from a single crystal. The studied material in these experiments is the nickel-based superalloy Allvac 718 Plus which is of special interest for the aerospace industry. In this thesis, the possibility to calibrate a crystal plasticity model based on data from microbeam bending experiments is investigated.

1.2 Thesis Objectives

The main purposes of this thesis are related to assisting in the establishment of a computational modeling platform for crystal plasticity at Chalmers. More specifically, a finite element model should be developed for Abaqus such that microbeam bending experiments can be simulated. An already implemented crystal plasticity user-defined material model (UMAT) is available as a user subroutine for Abaqus.

The finite element model should be generated from an Abaqus Python script to ensure a correct and consistent model setup. The model build-up from the script should be highly parametrized such that the user is able to specify microbeam dimensions, crystal orientation, material properties, mesh properties and

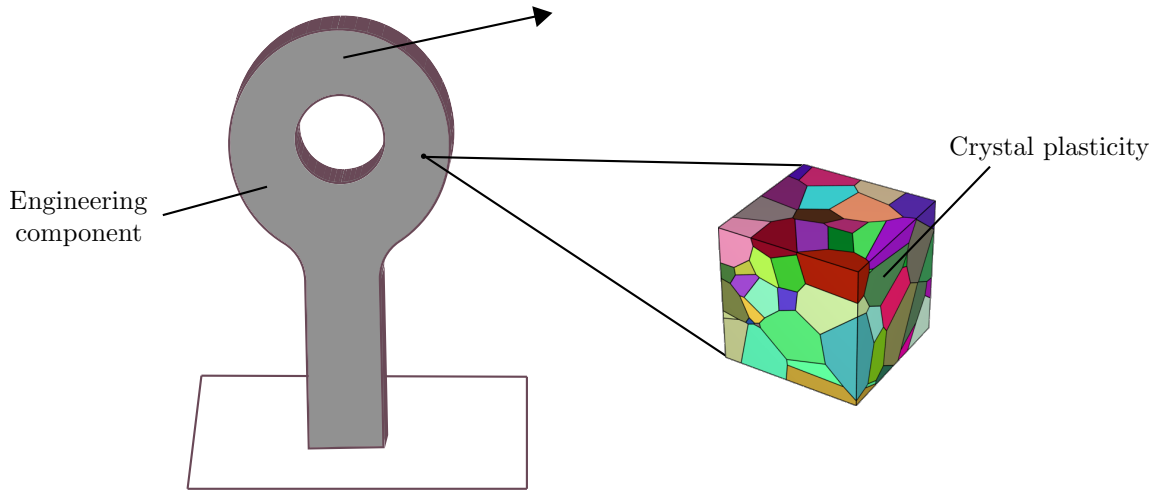

Figure 1.1: Illustration of multiscale modeling of metals.

some important analysis settings. It should also be possible to include an oxide layer on top of the microbeam structure.

Besides finite element model development, another objective is to develop a procedure in which microbeam simulations in Abaqus can be coupled with external optimization code. The optimization code should be able to make changes in material parameters and call new simulation jobs. The corresponding model response for given material parameters is then compared to experimental data as the definition of an objective function. The final task is to calibrate the crystal plasticity model based on the data from the microbeam bending experiments for the Allvac 718 Plus superalloy.

1.3 Report Structure

In Chapter 2, a description of the microbeam bending experiments is presented. This chapter covers the process of making microbeams, experiment setup and the experiment results. A presentation of crystal plasticity and the particular constitutive model used in the finite element modeling is given in Chapter 3. In Chapter 4, details about the finite element modeling of the experiments are presented. Chapter 5 treats calibration of the crystal plasticity model using the experimental data. The main report ends with Chapter 6 which mostly discusses the calibration results and suggestions for future work.

There are also two appendices. The first appendix contains some notes on Python scripting in Abaqus and explains the scripts used in the project. The second appendix treats the programming for the constitutive model calibration. It is in detailed covered how an external program, for example and in this case Matlab, may perform an engineering optimization task with underlying Abaqus simulations.

2 Microbeam Bending

The microbeam bending technique has been used by several authors, e.g. [2] and [3], to study the micromechanical properties of materials. This chapter covers the microbeam bending experiments including preparation and results. The work described here has been performed at the Department of Physics by Anand Harihara Subramonia Iyer. In total, three microbeams were made for the experiments. Each one of the microbeams is made out of a single crystal of the superalloy material Allvac 718 Plus. The three microbeams have different crystallographic orientation relative to a specified beam coordinate system. The crystal orientation for a microbeam affects its stiffness and the nature of its crystal slip. These effects of the crystal orientation are elaborated further on in Chapter 3.

The microbeams are shaped from a milling process using a FIB (focused ion beam) technique. Material is removed until the shape is satisfying and the beam structure looks like in the illustration in Figure 2.1. Since the milling process is a difficult one, the microbeam geometry measures will have some uncertainties. The geometry and orientation for each one of the three microbeams are given in Table 2.1 where the dimensions refer to Figure 2.1. The crystal orientations are presented in Euler angles using the Bunge convention. These angles are explained in detail in Section 3.2. The crystal orientations are measured with a technique called EBSD which is short for electron backscatter diffraction.

The experiment setup is illustrated in Figure 2.1. To prevent oxidation of the metal, the experiment is conducted in a vacuum environment. The whole specimen containing the grain of interest is attached to a spring table with a known stiffness (spring constant). The beam is then deflected by applying a point load with a diamond tip tool close to the tip of the beam. During the experiment, SEM (scanning electron microscope) images are recorded. The displacement of the whole specimen is measured from these images by tracking a first reference point, denoted A in Figure 2.1. The force applied in the diamond tip contact can then be evaluated from force equilibrium since the spring stiffness is known. In order for this concept to work, point A must belong to a non-deforming (or negligibly deforming) part of the specimen. The contact point B is tracked as well. By evaluating the displacement of point B relative to A, the beam deflection can be computed.

The experiment with microbeam B was successfully conducted. A force-deflection data plot for this experiment is given in Figure 2.2. Unfortunately, the experiments with microbeams A and C failed. For different reasons, these microbeams were not deformed in the way that was planned and no useful data was obtained. Images of the microbeams after the experiments are presented in Figure 2.3. Microbeams A and C (failed experiments) show signs of notable torsional deformation.

Table 2.1: Geometries and crystal orientations for the microbeams used in the experiments.

Experiment beams							
Beam	Geometry				Orientation		
	L (µm)	w (µm)	h (µm)	r (µm)	φ_1	Φ	φ_2
A	10.45	4.2	3.6	0.4	302.3°	40.7°	56.1°
B	13.0	3.0	3.9	0.11	79.3°	6.8°	36.9°
C	11.8	4.0	3.8	0.35	247.4°	41.9°	68.1°

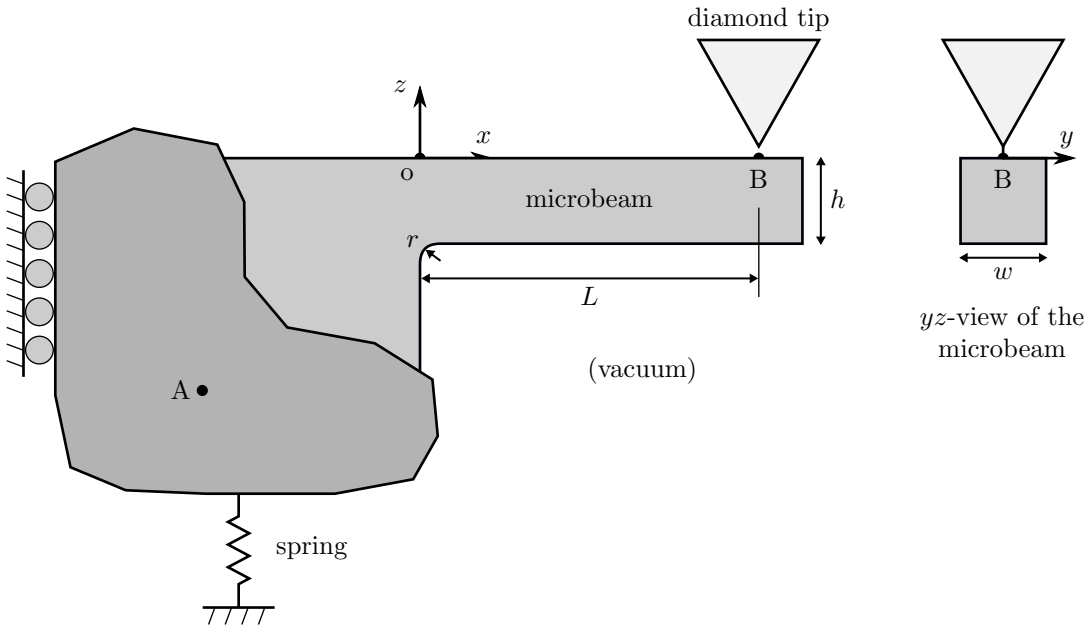

Figure 2.1: Illustration of the microbeam bending experiment setup and the microbeam dimensions.

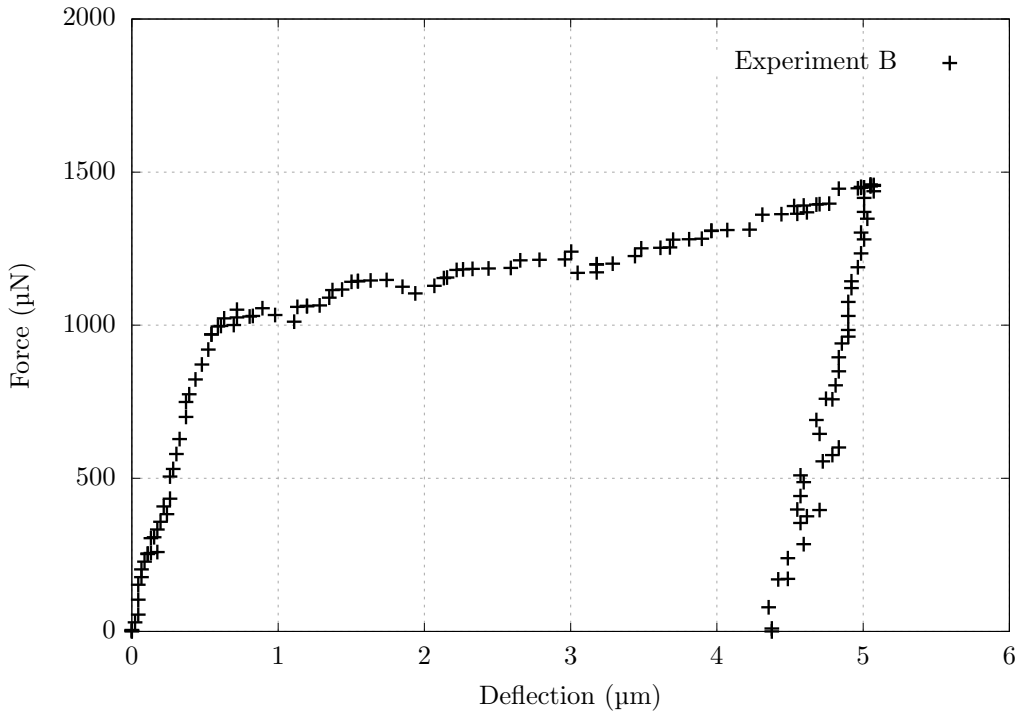

Figure 2.2: Force-deflection data from the successful experiment with microbeam B. Images for data evaluation was acquired once per second. The total time elapsed up to the point of unloading is approximately 100 seconds.

Microbeam A

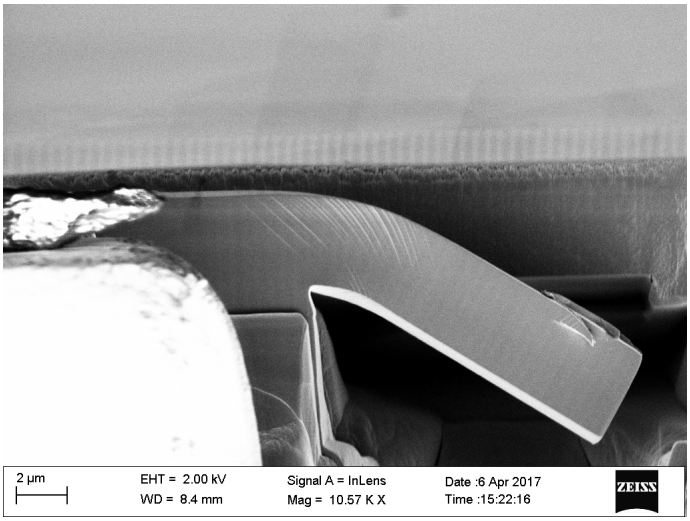

Microbeam B

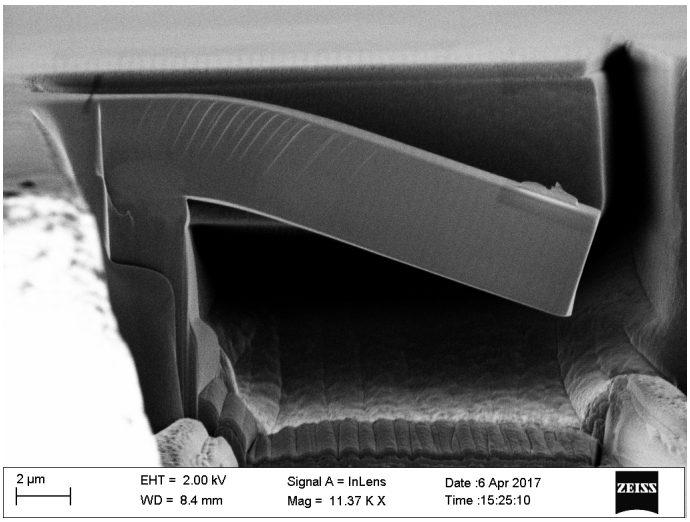

Microbeam C

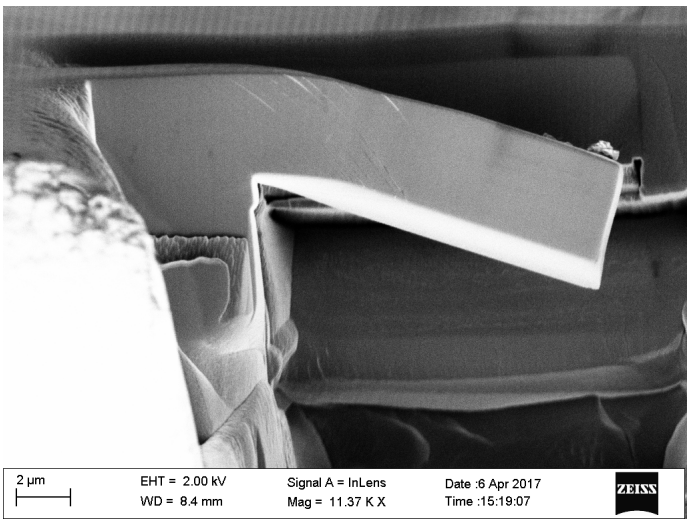

Figure 2.3: SEM images from an xz-view of microbeams A, B and C after the experiments.

3 Crystal Plasticity

A thorough overview of the basics of crystal plasticity modeling is given in e.g. Reference [4]. Here, only the main modeling features are presented. For clarity of presentation, the crystal plasticity model formulation is here restricted to small strains. However, the simulation results in this report are produced using a corresponding formulation based on the finite strain theory (large strains).

3.1 Notations

First-order tensors or vectors will be denoted by bold-faced and upright italic characters, e.g. $\mathbf{a}$ or $\mathbf{b}$. Some bold-faced greek characters represent second-order tensors, like the Cauchy stress tensor $\boldsymbol{\sigma}$ and the strain tensor $\boldsymbol{\epsilon}$. Bold-faced and calligraphic capital characters will represent tensors of order four. Examples of fourth-order tensors are the elastic stiffness modulus tensor $\boldsymbol{\mathcal{C}}$ and the related compliance tensor $\boldsymbol{\mathcal{C}}^{-1}$. Whenever components of tensors are used in expressions, e.g. σ_{ij}, these refer to a Cartesian coordinate system.

Regarding tensor operations, $\otimes$ will be used to denote the open product. Scalar product or single contraction is denoted by a single dot $\cdot$, whereas : is used for double contraction. An example of double contraction is given by

$$\boldsymbol{\mathcal{C}} : \boldsymbol{\epsilon} = \mathcal{C}_{ijkl}\epsilon_{kl}\,\mathbf{e}_i \otimes \mathbf{e}_j. \tag{3.1}$$

3.2 Crystal Orientations

Since single crystals in general are anisotropic, it is important to properly describe their orientations. This is commonly achieved by using Euler angles with the Bunge convention. Throughout this report, the global reference coordinate system is denoted by $oxyz$ whereas the crystal material coordinate system is given by $ox'y'z'$. The corresponding unit basis vectors are denoted $\{\mathbf{e}_i\}_{i=1}^3 = \{\mathbf{e}_1, \mathbf{e}_2, \mathbf{e}_3\}$ and $\{\mathbf{e}'_i\}_{i=1}^3 = \{\mathbf{e}'_1, \mathbf{e}'_2, \mathbf{e}'_3\}$, respectively.

3.2.1 Euler Angles (Bunge Convention)

Euler angles represent three finite consecutive rotations and are used to describe the orientation of a body relative to some fixed coordinate system [5]. The Bunge convention for the Euler angles is illustrated in Figure 3.1 with angles given by φ_1, Φ and φ_2. A description of the three rotations with the Bunge system follows below in which the vectors refer to Figure 3.1.

1. Rotation by an angle $\varphi_1 \in [-180°, 180°]$ about the x_3-axis which gives the rotated basis vectors

$$\begin{aligned} \mathbf{e}_1^{(1)} &= \cos\varphi_1\,\mathbf{e}_1 + \sin\varphi_1\,\mathbf{e}_2, \\ \mathbf{e}_2^{(1)} &= -\sin\varphi_1\,\mathbf{e}_1 + \cos\varphi_1\,\mathbf{e}_2, \\ \mathbf{e}_3^{(1)} &= \mathbf{e}_3. \end{aligned} \tag{3.2}$$

2. Rotation by an angle $\Phi \in [0°, 180°]$ about the $x_1^{(1)}$-axis obtained from the first rotation. The new coordinate system has the basis vectors

$$\begin{aligned} \mathbf{e}_1^{(2)} &= \mathbf{e}_1^{(1)}, \\ \mathbf{e}_2^{(2)} &= \cos\Phi\,\mathbf{e}_2^{(1)} + \sin\Phi\,\mathbf{e}_3^{(1)}, \\ \mathbf{e}_3^{(2)} &= -\sin\Phi\,\mathbf{e}_2^{(1)} + \cos\Phi\,\mathbf{e}_3^{(1)}. \end{aligned} \tag{3.3}$$

3. Final rotation by an angle $\varphi_2 \in [-180°, 180°]$ about the $x_3^{(2)}$-axis yields basis vectors for the crystal material axes:

$$\begin{aligned} \mathbf{e}'_1 = \mathbf{e}_1^{(3)} &= \cos\varphi_2\,\mathbf{e}_1^{(2)} + \sin\varphi_2\,\mathbf{e}_2^{(2)}, \\ \mathbf{e}'_2 = \mathbf{e}_2^{(3)} &= -\sin\varphi_2\,\mathbf{e}_1^{(2)} + \cos\varphi_2\,\mathbf{e}_2^{(2)}, \\ \mathbf{e}'_3 = \mathbf{e}_3^{(3)} &= \mathbf{e}_3^{(2)}. \end{aligned} \tag{3.4}$$

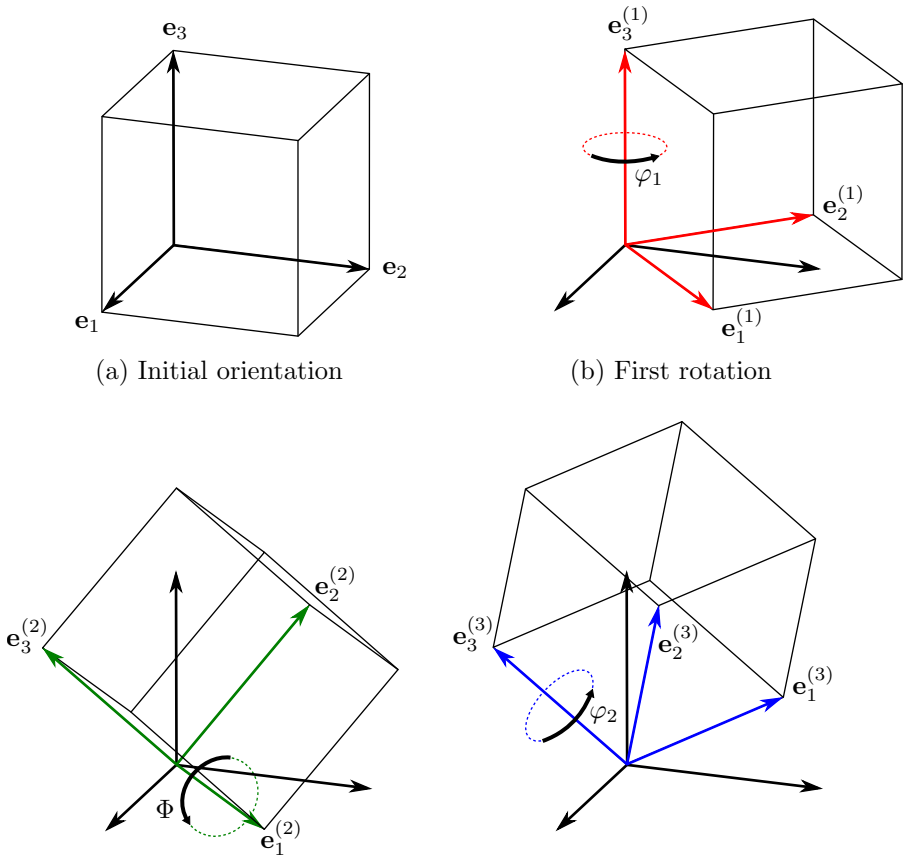

(a) Initial orientation (b) First rotation

(c) Second rotation (d) Third rotation

Figure 3.1: Illustration of the cubic crystal orientation using Euler angles with the Bunge convention.

In summary, the transformation of the basis vectors from oxyz to o$x'y'z'$ using the Bunge convention may be described by the matrix formulation

$$\begin{bmatrix}\mathbf{e}'_1 & \mathbf{e}'_2 & \mathbf{e}'_3\end{bmatrix} = \begin{bmatrix}\mathbf{e}_1 & \mathbf{e}_2 & \mathbf{e}_3\end{bmatrix} \mathbf{R}_{\varphi_1}\mathbf{R}_{\Phi}\,\mathbf{R}_{\varphi_2} \tag{3.5}$$

where

$$\mathbf{R}_{\varphi_1} = \begin{bmatrix}\cos\varphi_1 & -\sin\varphi_1 & 0\\ \sin\varphi_1 & \cos\varphi_1 & 0\\ 0 & 0 & 1\end{bmatrix}, \quad \mathbf{R}_{\Phi} = \begin{bmatrix}1 & 0 & 0\\ 0 & \cos\Phi & -\sin\Phi\\ 0 & \sin\Phi & \cos\Phi\end{bmatrix}, \quad \mathbf{R}_{\varphi_2} = \begin{bmatrix}\cos\varphi_2 & -\sin\varphi_2 & 0\\ \sin\varphi_2 & \cos\varphi_2 & 0\\ 0 & 0 & 1\end{bmatrix}. \tag{3.6}$$

3.2.2 Rotation Matrix

A rotation matrix, commonly denoted $\mathbf{Q}$, may be used to transform coordinates from one coordinate system to a rotated coordinate system. The components of $\mathbf{Q}$ are defined as projections of the basis vectors between the two coordinate systems. For transformations between the two coordinate systems oxyz and o$x'y'z'$, we may define the components of $\mathbf{Q}$ as

$$Q_{ij} = \mathbf{e}'_i \cdot \mathbf{e}_j\,. \tag{3.7}$$

Using Euler angles with the Bunge convention, the transposed rotation matrix is obtained as

$$\mathbf{Q}^{\mathrm{T}} = \begin{bmatrix}\mathbf{e}_1^{\mathrm{T}}\\ \mathbf{e}_2^{\mathrm{T}}\\ \mathbf{e}_3^{\mathrm{T}}\end{bmatrix}\begin{bmatrix}\mathbf{e}'_1 & \mathbf{e}'_2 & \mathbf{e}'_3\end{bmatrix} = \begin{bmatrix}\mathbf{e}_1^{\mathrm{T}}\\ \mathbf{e}_2^{\mathrm{T}}\\ \mathbf{e}_3^{\mathrm{T}}\end{bmatrix}\begin{bmatrix}\mathbf{e}_1 & \mathbf{e}_2 & \mathbf{e}_3\end{bmatrix}\mathbf{R}_{\varphi_1}\mathbf{R}_{\Phi}\,\mathbf{R}_{\varphi_2} = \mathbf{R}_{\varphi_1}\mathbf{R}_{\Phi}\,\mathbf{R}_{\varphi_2} \tag{3.8}$$

where the orthonormality of the vectors $\{\mathbf{e}_i\}_{i=1}^3$ was used in the last equality. Equation (3.8) implies that

$$\mathbf{Q} = \left(\mathbf{R}_{\varphi_1}\mathbf{R}_{\Phi}\,\mathbf{R}_{\varphi_2}\right)^{\mathrm{T}} = \mathbf{R}_{\varphi_2}^{\mathrm{T}}\mathbf{R}_{\Phi}^{\mathrm{T}}\,\mathbf{R}_{\varphi_1}^{\mathrm{T}}. \tag{3.9}$$

Carrying out the matrix multiplication using the matrices in (3.6), we finally end up with

$$\mathbf{Q} = \begin{bmatrix}\cos\varphi_1\cos\varphi_2 - \sin\varphi_1\cos\Phi\sin\varphi_2 & \sin\varphi_1\cos\varphi_2 + \cos\varphi_1\cos\Phi\sin\varphi_2 & \sin\Phi\sin\varphi_2\\ -\cos\varphi_1\sin\varphi_2 - \sin\varphi_1\cos\Phi\cos\varphi_2 & -\sin\varphi_1\sin\varphi_2 + \cos\varphi_1\cos\Phi\cos\varphi_2 & \sin\Phi\cos\varphi_2\\ \sin\varphi_1\sin\Phi & -\cos\varphi_1\sin\Phi & \cos\Phi\end{bmatrix}. \tag{3.10}$$

3.2.3 Tensor Transformations

Working with arbitrary crystallographic orientation, it is necessary to be able to carry out transformations of tensors. Consider the two coordinate systems oxyz and o$x'y'z'$ (both orthonormal) for which the corresponding basis vectors are given by $\{\mathbf{e}_i\}_{i=1}^3$ and $\{\mathbf{e}'_i\}_{i=1}^3$, respectively. A first-order tensor $\mathbf{a}$ may be represented in these two coordinate systems accordingly:

$$\mathbf{a} = a_i\,\mathbf{e}_i = a'_j\,\mathbf{e}'_j\,. \tag{3.11}$$

The component a'_i is given by projecting $\mathbf{a}$ onto $\mathbf{e}'_i$, i.e.

$$a'_i = \mathbf{a}\cdot\mathbf{e}'_i = (a_j\,\mathbf{e}_j)\cdot\mathbf{e}'_i = Q_{ji}^{\mathrm{T}}a_j = Q_{ij}a_j \tag{3.12}$$

where the components of the rotation matrix $\mathbf{Q}$ were used in the last two equalities, here interpreted as a tensor. The reverse projection may be set up in the same way:

$$a_i = \mathbf{a}\cdot\mathbf{e}_i = (a'_j\,\mathbf{e}'_j)\cdot\mathbf{e}_i = Q_{ji}a'_j = Q_{ij}^{\mathrm{T}}a'_j\,. \tag{3.13}$$

Transformations of higher order tensors follow the same pattern. For instance, the transformations of the fourth-order stiffness tensor $\boldsymbol{\mathcal{C}} = C_{ijkl}\,\mathbf{e}_i\otimes\mathbf{e}_j\otimes\mathbf{e}_k\otimes\mathbf{e}_l = C'_{mnop}\,\mathbf{e}'_m\otimes\mathbf{e}'_n\otimes\mathbf{e}'_o\otimes\mathbf{e}'_p$ are given by

$$C'_{ijkl} = Q_{im}Q_{jn}Q_{ko}Q_{lp}C_{mnop} \tag{3.14}$$

and

$$C_{ijkl} = Q_{im}^{\mathrm{T}}Q_{jn}^{\mathrm{T}}Q_{ko}^{\mathrm{T}}Q_{lp}^{\mathrm{T}}C'_{mnop}\,. \tag{3.15}$$

3.3 Elastic Cubic Symmetry

Linear elastic cubic symmetry is an appropriate assumption for the elastic behavior of a cubic crystal, c.f. [6]. Apart from the crystal orientation, three elastic material constants are needed in order to describe the stress-strain relationship $\boldsymbol{\sigma} = \boldsymbol{\mathcal{C}} : \boldsymbol{\epsilon}$ in elastic cubic symmetry. These three parameters are commonly denoted C_{11}, C_{12} and C_{44}. The stiffness tensor for elastic cubic symmetry may be expressed in Voigt form as

$$\left[\boldsymbol{\mathcal{C}}'\right] = \begin{bmatrix} C_{11} & C_{12} & C_{12} & 0 & 0 & 0 & 0 & 0 & 0 \\ C_{12} & C_{11} & C_{12} & 0 & 0 & 0 & 0 & 0 & 0 \\ C_{12} & C_{12} & C_{11} & 0 & 0 & 0 & 0 & 0 & 0 \\ 0 & 0 & 0 & 2\,C_{44} & 0 & 0 & 0 & 0 & 0 \\ 0 & 0 & 0 & 0 & 2\,C_{44} & 0 & 0 & 0 & 0 \\ 0 & 0 & 0 & 0 & 0 & 2\,C_{44} & 0 & 0 & 0 \\ 0 & 0 & 0 & 0 & 0 & 0 & 2\,C_{44} & 0 & 0 \\ 0 & 0 & 0 & 0 & 0 & 0 & 0 & 2\,C_{44} & 0 \\ 0 & 0 & 0 & 0 & 0 & 0 & 0 & 0 & 2\,C_{44} \end{bmatrix}. \tag{3.16}$$

The prime superscript $'$ on $\boldsymbol{\mathcal{C}}$ in (3.16) is used to stress the fact the components refer to the material coordinates $\mathrm{o}x'y'z'$.

3.3.1 Apparent Young's Modulus

The concept of apparent Young's modulus can be used to illustrate elastic cubic symmetry. Now, let $\mathbf{n}$ be an arbitrary unit vector. The apparent Young's modulus $E_{\mathbf{n}}$ relates the normal stress and normal strain in the direction $\mathbf{n}$ for the case of uniaxial stress condition along $\mathbf{n}$. This relation is given by

$$\sigma_{\mathbf{n}} = E_{\mathbf{n}} \epsilon_{\mathbf{n}} \tag{3.17}$$

where

$$\sigma_{\mathbf{n}} = \boldsymbol{\sigma} : (\mathbf{n} \otimes \mathbf{n}), \quad \epsilon_{\mathbf{n}} = \boldsymbol{\epsilon} : (\mathbf{n} \otimes \mathbf{n}). \tag{3.18}$$

By substituting (3.18) in (3.17) and using $\boldsymbol{\epsilon} = \boldsymbol{\mathcal{C}}^{-1} : \boldsymbol{\sigma} = \boldsymbol{\sigma} : \boldsymbol{\mathcal{C}}^{-1}$, we obtain

$$\boldsymbol{\sigma} : (\mathbf{n} \otimes \mathbf{n}) = E_{\mathbf{n}}\, \boldsymbol{\epsilon} : (\mathbf{n} \otimes \mathbf{n}) = E_{\mathbf{n}}\, \boldsymbol{\sigma} : \boldsymbol{\mathcal{C}}^{-1} : (\mathbf{n} \otimes \mathbf{n}) \tag{3.19}$$

which implies that

$$(\mathbf{n} \otimes \mathbf{n}) = E_{\mathbf{n}}\, \boldsymbol{\mathcal{C}}^{-1} : (\mathbf{n} \otimes \mathbf{n}). \tag{3.20}$$

Performing a double dot contraction by $\mathbf{n} \otimes \mathbf{n}$ from the left on both sides, we find the apparent Young's modulus $E_{\mathbf{n}}$ from the equation

$$\frac{1}{E_{\mathbf{n}}} = (\mathbf{n} \otimes \mathbf{n}) : \boldsymbol{\mathcal{C}}^{-1} : (\mathbf{n} \otimes \mathbf{n}). \tag{3.21}$$

As adopted from [7], varying the two first Bunge angles φ_1 and Φ, we obtain the apparent Young's modulus plotted in Figure 3.2 along the beam axis. To produce this plot, the following representation of the vector $\mathbf{n}$ was substituted in Equation (3.21):

$$\mathbf{n} = \begin{bmatrix} \cos\phi\, \sin\theta \\ \sin\phi\, \sin\theta \\ \cos\theta \end{bmatrix} \tag{3.22}$$

where angles ϕ and θ refer to the polar coordinates used in Figure 3.2. For the elastic material parameters we have here used $C_{11} = 259.6\,\mathrm{GPa}$, $C_{12} = 179.0\,\mathrm{GPa}$ and $C_{44} = 109.6\,\mathrm{GPa}$.

3.4 Crystal Plasticity

3.4.1 Slip Systems

The plastic deformation of the crystal lattice, called slip, is more prone to occur in certain planes and directions due to the packing of atoms. The slip corresponds to movement of dislocations that is activated by high shear

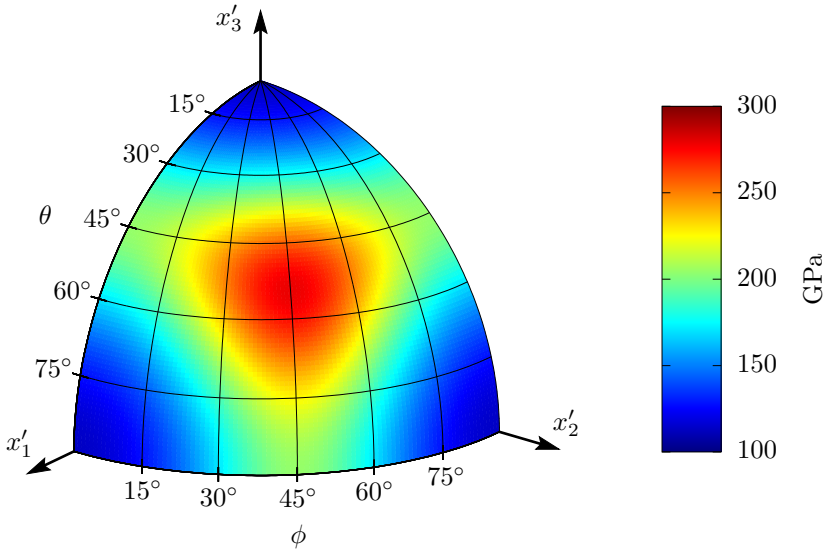

Figure 3.2: The concept of apparent Young's modulus for a crystal illustrated in spherical coordinates. Maximum is obtained for direction with Miller index [1 1 1] which corresponds to $\phi = 45.00°$ and $\theta = 54.74°$.

stress levels. The easiest movement of dislocations, i.e. movement activated by relatively low shear stress levels, occur in the planes and directions with the highest density of atoms. These slip directions and planes are often referred to as "close-packed" directions and planes.

The slip mechanism is modeled using a set of slip systems. Each slip system α is described by a slip direction $\mathbf{s}^\alpha$ and a corresponding slip plane described by its normal $\mathbf{m}^\alpha$. In total, a set of N_{slip} slip systems $\{(\mathbf{s}^\alpha, \mathbf{m}^\alpha)\}_{\alpha=1}^{N_{\text{slip}}}$ are considered for the crystal. The superalloys of interest in this thesis, Allvac 718 Plus and the similar Inconel 718, both have a face centered cubic (FCC) crystal structure [1]. For an FCC crystal, see Figure 3.3a, the slip planes have members in the Miller index family $\{1\ 1\ 1\}$ and the slip directions belong to the family $\langle 1\ 1\ 0 \rangle$. The slip system family for an FCC crystal is illustrated in Figure 3.3b. All 12 slip systems for an FCC crystal are presented in Table 3.1. If slip for a body centered cubic (BCC) crystal is to be modeled instead, these would need to be substituted.

Table 3.1: The planes and directions of the 12 slip systems for an FCC crystal given in both Miller indices and vector format (local crystal coordinates).

Slip system α	Plane		Direction	
	Miller index	Normal vector $\mathbf{m}^\alpha$	Miller index	Vector $\mathbf{s}^\alpha$
1	$(1\ 1\ 1)$	$(1,1,1)/\sqrt{3}$	$[\bar{1}\ 1\ 0]$	$(-1,1,0)/\sqrt{2}$
2	$(1\ 1\ 1)$	$(1,1,1)/\sqrt{3}$	$[0\ \bar{1}\ 1]$	$(0,-1,1)/\sqrt{2}$
3	$(1\ 1\ 1)$	$(1,1,1)/\sqrt{3}$	$[1\ 0\ \bar{1}]$	$(1,0,-1)/\sqrt{2}$
4	$(\bar{1}\ 1\ 1)$	$(-1,1,1)/\sqrt{3}$	$[\bar{1}\ \bar{1}\ 0]$	$(-1,-1,0)/\sqrt{2}$
5	$(\bar{1}\ 1\ 1)$	$(-1,1,1)/\sqrt{3}$	$[1\ 0\ 1]$	$(1,0,1)/\sqrt{2}$
6	$(\bar{1}\ 1\ 1)$	$(-1,1,1)/\sqrt{3}$	$[0\ 1\ \bar{1}]$	$(0,1,-1)/\sqrt{2}$
7	$(1\ \bar{1}\ 1)$	$(1,-1,1)/\sqrt{3}$	$[1\ 1\ 0]$	$(1,1,0)/\sqrt{2}$
8	$(1\ \bar{1}\ 1)$	$(1,-1,1)/\sqrt{3}$	$[\bar{1}\ 0\ 1]$	$(-1,0,1)/\sqrt{2}$
9	$(1\ \bar{1}\ 1)$	$(1,-1,1)/\sqrt{3}$	$[0\ \bar{1}\ \bar{1}]$	$(0,-1,-1)/\sqrt{2}$
10	$(1\ 1\ \bar{1})$	$(1,1,-1)/\sqrt{3}$	$[1\ \bar{1}\ 0]$	$(1,-1,0)/\sqrt{2}$
11	$(1\ 1\ \bar{1})$	$(1,1,-1)/\sqrt{3}$	$[\bar{1}\ 0\ \bar{1}]$	$(-1,0,-1)/\sqrt{2}$
12	$(1\ 1\ \bar{1})$	$(1,1,-1)/\sqrt{3}$	$[0\ 1\ 1]$	$(0,1,1)/\sqrt{2}$

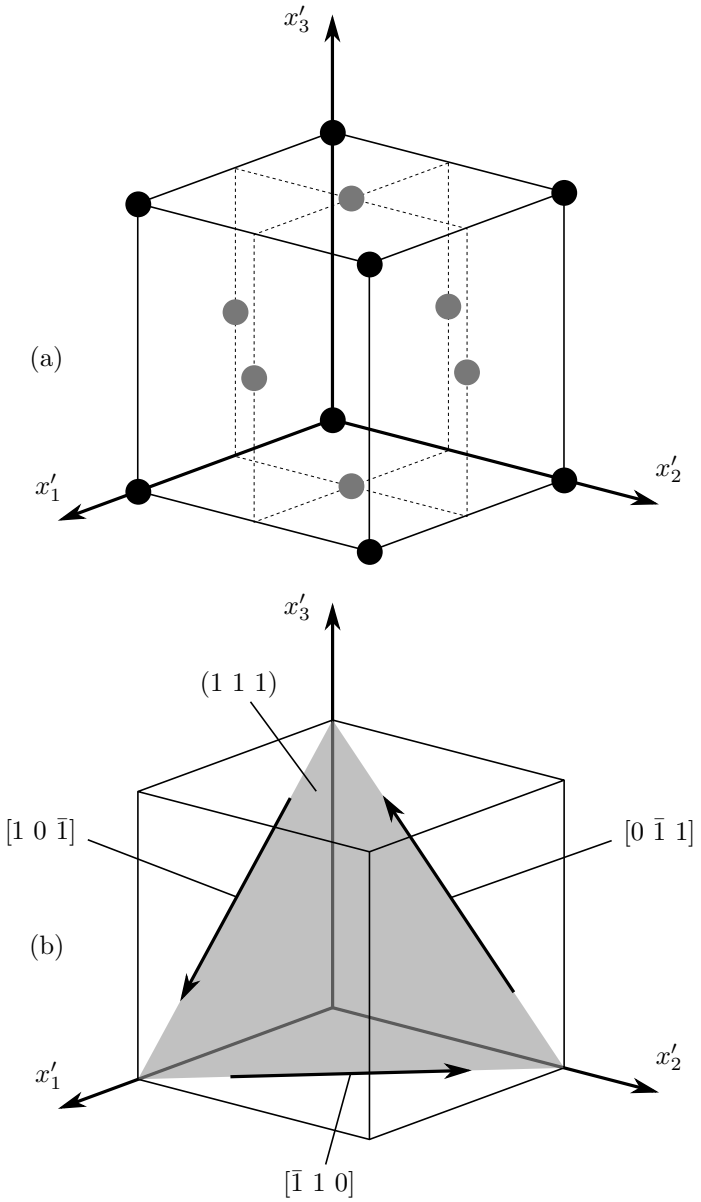

Figure 3.3: (a) Illustration of the atom structure in an FCC crystal. (b) Unit cell illustration of the three slip systems associated with the plane (1 1 1) for an FCC crystal.

3.4.2 Governing Equations

The crystal plasticity model used for the simulations in this thesis is adopted from Reference [8]. This material model is based on the finite strain theory. For clarity, the formulation is here presented in a corresponding small strain formulation.

The traction vector $\mathbf{t}^\alpha$ on the slip plane associated with slip system α is obtained by projection of the stress tensor $\boldsymbol{\sigma}$ onto the corresponding slip plane normal $\mathbf{m}^\alpha$, i.e.

$$\mathbf{t}^\alpha = \boldsymbol{\sigma} \cdot \mathbf{m}^\alpha. \tag{3.23}$$

The projected or resolved shear stress in the slip direction, also known as the Schmid stress, is denoted τ_α and is given by

$$\tau_\alpha = \mathbf{t}^\alpha \cdot \mathbf{s}^\alpha = \boldsymbol{\sigma} : (\mathbf{m}^\alpha \otimes \mathbf{s}^\alpha)\,. \tag{3.24}$$

The evolution of the plastic strain $\boldsymbol{\epsilon}^{\mathrm{p}}$ is assumed to follow the law

$$\dot{\boldsymbol{\epsilon}}^{\mathrm{p}} = \sum_{\alpha=1}^{N_{\mathrm{slip}}} \dot{\gamma}_\alpha \left(\mathbf{m}^\alpha \otimes \mathbf{s}^\alpha\right)^{\mathrm{sym}} \frac{\tau_\alpha}{|\tau_\alpha|} \tag{3.25}$$

where

$$\dot{\gamma}_\alpha = \dot{\gamma}_0 \left(\frac{|\tau_\alpha|}{\tau_\alpha^{\mathrm{c}}}\right)^{1/m} \mathrm{sign}(\tau_\alpha) \quad \alpha = 1, 2, \ldots, N_{\mathrm{slip}}. \tag{3.26}$$

The variable τ_α^{c} is called the critical resolved shear stress associated with slip system α. The evolution of τ_α^{c} is given by

$$\dot{\tau}_\alpha^c = \sum_{\beta=1}^{N_{\mathrm{slip}}} q_{\alpha\beta}\, h(\gamma)\, |\dot{\gamma}_\beta| \quad \alpha = 1, 2, \ldots, N_{\mathrm{slip}}. \tag{3.27}$$

In Equation (3.27), the Voce hardening model $h(\gamma)$ was introduced and is given by

$$h(\gamma) = h_\infty + \left[h_0 - h_\infty + \frac{h_0 h_\infty \gamma}{\tau_\infty - \tau_0}\right] \exp\left(-\frac{h_0 \gamma}{\tau_\infty - \tau_0}\right) \tag{3.28}$$

where γ refers to the accumulated slip among all slip systems, i.e.

$$\gamma(t) = \int_0^t \sum_{\alpha=1}^{N_{\mathrm{slip}}} |\dot{\gamma}_\alpha|\, \mathrm{d}t\,. \tag{3.29}$$

The plasticity part of the constitutive model introduces the 8 parameters $\dot{\gamma}_0$, m, h_∞, h_0, τ_∞, τ_0, $q_{\alpha\alpha}$ and $q_{\alpha\beta}$. To fully define the constitutive model we also need the Bunge angles (φ_1, Φ and φ_2), the elastic parameters (C_{11}, C_{12} and C_{44}) and the slip systems (Table 3.1).

3.4.3 Yield Surface Interpretation

Although the crystal plasticity formulation in the previous subsection is given as a viscoelastic regularization, we may still interpret a "yield surface" by comparing the Schmid stress τ_α between the slip systems. The plane stress situation in which the normal stresses are equal to the principal stresses (no shear stresses) is plotted in Figure 3.4 for different coordinate systems relative to the crystal material axes. The Cauchy stress tensor expressed in the rotated Cartesian coordinate system defined by ϕ is given by

$$[\boldsymbol{\sigma}_\phi] = \begin{bmatrix} \sigma_1 & 0 & 0 \\ 0 & \sigma_2 & 0 \\ 0 & 0 & 0 \end{bmatrix}. \tag{3.30}$$

The nonsmooth transitions or "kinks" in Figure 3.4 represent changes of slip system corresponding to the largest Schmid stress τ_α.

3.5 Implementation

Crystal plasticity material models are typically not included commercial finite element software. However, some of the more sophisticated commercial finite element codes, like Abaqus which is used in this thesis, provide the capability for the user to incorporate own code into the analysis. For Abaqus, user provided code is referred to as user subroutines. Within the framework of user subroutines in Abaqus, it is possible to define a user-defined material model which is called UMAT [9]. User subroutines are commonly written in the Fortran language, but C++ is an option as well .

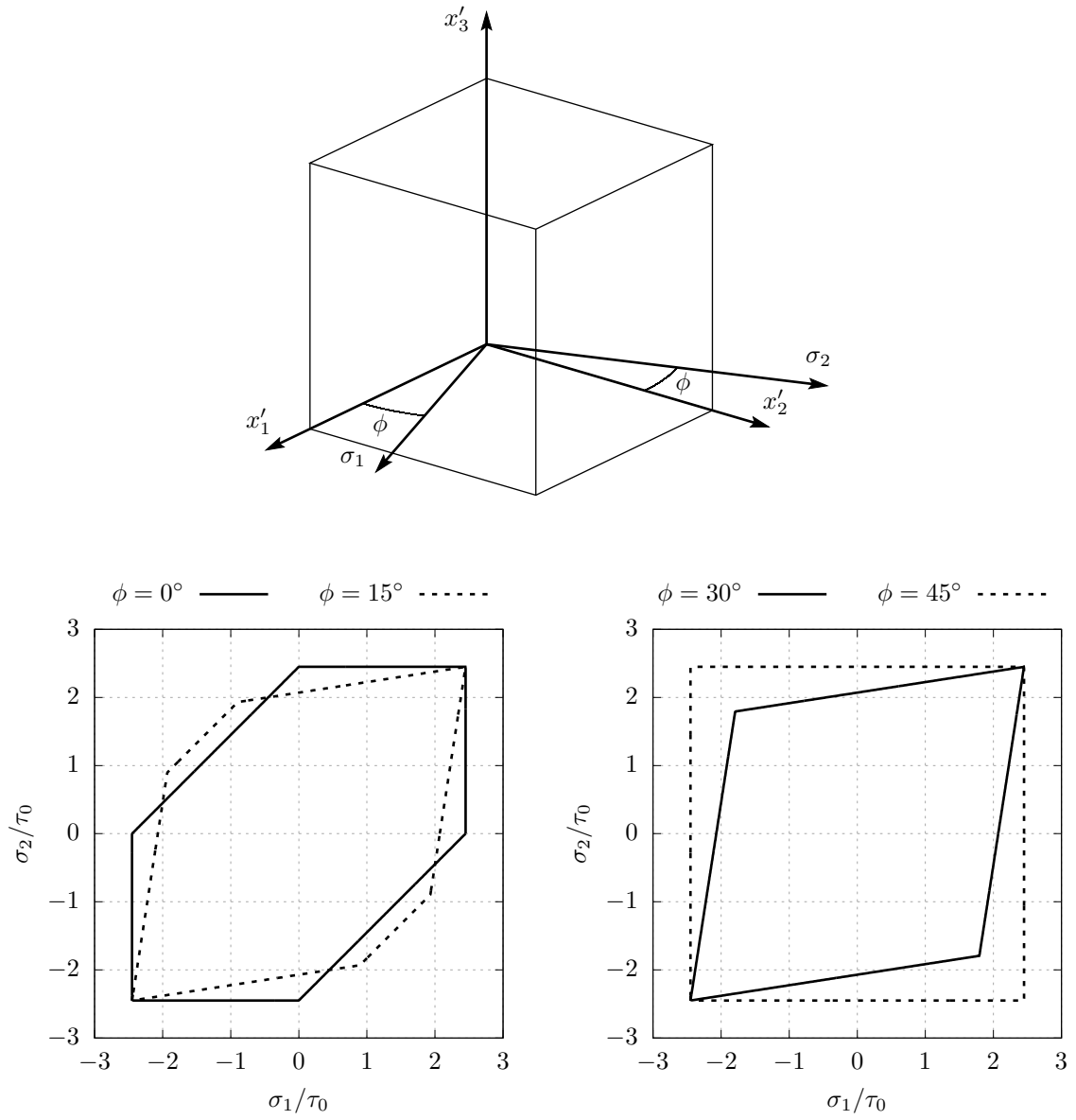

Figure 3.4: Plane stress yield surface interpretations for a principal stress condition obtained for the crystal plasticity model. The principal stress axes are defined by the angle ϕ relative the crystal material axes. Plane stress is given by the condition $\sigma_3 = 0$.

3.5.1 Local Constitutive Problem

The evolution is governed by the following system of equations

$$\begin{cases} \dot{\boldsymbol{\sigma}} = \boldsymbol{\mathcal{E}}^{\mathrm{e}} : (\dot{\boldsymbol{\epsilon}} - \dot{\boldsymbol{\epsilon}}^{\mathrm{p}}) , \\ \dot{\boldsymbol{\epsilon}}^{\mathrm{p}} = \displaystyle\sum_{\alpha=1}^{N_{\mathrm{slip}}} \dot{\gamma}_\alpha \left(\mathbf{s}_\alpha \otimes \mathbf{m}_\alpha\right)^{\mathrm{sym}} , \\ \dot{\gamma}_\alpha = \dot{\gamma}_0 \left(\dfrac{|\tau_\alpha|}{\tau_\alpha^{\mathrm{c}}} \right)^{1/m} \mathrm{sign}(\tau_\alpha) \quad \alpha = 1, 2, \ldots, N_{\mathrm{slip}}, \\ \dot{\tau}_\alpha^{c} = \displaystyle\sum_{\beta=1}^{N_{\mathrm{slip}}} q_{\alpha\beta}\, h(\gamma)\, |\dot{\gamma}_\beta| \quad \alpha = 1, 2, \ldots, N_{\mathrm{slip}}, \\ \tau_\alpha = \boldsymbol{\sigma} : (\mathbf{s}^\alpha \otimes \mathbf{m}^\alpha) \quad \alpha = 1, 2, \ldots, N_{\mathrm{slip}}. \end{cases} \tag{3.31}$$

Using an indirect or implicit solution strategy, these equations are integrated with respect to time using the backward Euler method. The variables are assumed to be known at time t_n and integrated to t_{n+1} which gives us a time step $\Delta t = t_{n+1} - t_n$. Any state variable value corresponding to time t_n or t_{n+1} will be denoted by a superscript in front of the variable. For example, for the strain we would use ${}^{n}\boldsymbol{\epsilon}$ and ${}^{n+1}\boldsymbol{\epsilon}$. Changes in state variables between t_n and t_{n+1} will be denoted by the symbol Δ, e.g. $\Delta\boldsymbol{\epsilon} = {}^{n+1}\boldsymbol{\epsilon} - {}^{n}\boldsymbol{\epsilon}$. Integrating the evolution equations in (3.31) using the backward Euler method, we obtain

$$\begin{cases} {}^{n+1}\boldsymbol{\sigma} = {}^{n}\boldsymbol{\sigma} + \boldsymbol{\mathcal{E}}^{\mathrm{e}} : (\Delta\boldsymbol{\epsilon} - \Delta\boldsymbol{\epsilon}^{\mathrm{p}}) , \\ \Delta\boldsymbol{\epsilon}^{\mathrm{p}} = \displaystyle\sum_{\alpha=1}^{N_{\mathrm{slip}}} \Delta\gamma_\alpha \left(\mathbf{s}^\alpha \otimes \mathbf{m}^\alpha\right)^{\mathrm{sym}} , \\ \Delta\gamma_\alpha = \dot{\gamma}_0\, \Delta t \left(\dfrac{|{}^{n+1}\tau_\alpha|}{{}^{n+1}\tau_\alpha^{\mathrm{c}}} \right)^{1/m} \mathrm{sign}({}^{n+1}\tau_\alpha) \quad \alpha = 1, 2, \ldots, N_{\mathrm{slip}}, \\ {}^{n+1}\tau_\alpha^{\mathrm{c}} = {}^{n}\tau_\alpha^{\mathrm{c}} + \displaystyle\sum_{\beta=1}^{N_{\mathrm{slip}}} q_{\alpha\beta}\, h({}^{n+1}\gamma)\, |\Delta\gamma_\beta| \quad \alpha = 1, 2, \ldots, N_{\mathrm{slip}}, \\ {}^{n+1}\tau_\alpha = {}^{n+1}\boldsymbol{\sigma} : (\mathbf{s}^\alpha \otimes \mathbf{m}^\alpha) \quad \alpha = 1, 2, \ldots, N_{\mathrm{slip}}. \end{cases} \tag{3.32}$$

As part of the finite element (global) iterations, the constitutive equations should be formulated in a strain-driven format. In a strain-driven format, $\Delta\boldsymbol{\epsilon}$ and the old state variables are given from the finite element code and the updated stress, stiffness tensors and state variables should be computed. Hence, $\Delta\boldsymbol{\epsilon}^{\mathrm{p}}$ is the only unknown on the right hand side of (3.32.1). Variable $\Delta\boldsymbol{\epsilon}^{\mathrm{p}}$ can in turn be computed from (3.32.2) as soon as $\{\Delta\gamma_\alpha\}_{\alpha=1}^{N_{\mathrm{slip}}}$ are known. The slip system plane normals $\{\mathbf{m}\}_{\alpha=1}^{N_{\mathrm{slip}}}$ and directions $\{\mathbf{s}\}_{\alpha=1}^{N_{\mathrm{slip}}}$ remain constant throughout the analysis in a small strain formulation. The residual problem set up to determine $\{\Delta\gamma_\alpha\}_{\alpha=1}^{N_{\mathrm{slip}}}$ can be described by the N_{slip} scalar equations

$$\mathcal{R}_\alpha(\{\Delta\gamma_\beta\}) = \Delta\gamma_\alpha - \dot{\gamma}_0\, \Delta t \left(\frac{|{}^{n+1}\tau_\alpha(\{\Delta\gamma_\beta\})|}{{}^{n+1}\tau_\alpha^{\mathrm{c}}(\{\Delta\gamma_\beta\})} \right)^{1/m} \mathrm{sign}\left[{}^{n+1}\tau_\alpha(\{\Delta\gamma_\beta\})\right] = 0 \quad \alpha = 1, 2, \ldots, N_{\mathrm{slip}} \tag{3.33}$$

where we let $\{\Delta\gamma_\beta\} = \{\Delta\gamma_\beta\}_{\beta=1}^{N_{\mathrm{slip}}}$ in short, i.e. the set of updates of the slip variables.

Newton's method can be employed to iteratively solve the local constitutive residual problem in Equation (3.33). We now introduce the definitions

$$\underline{\boldsymbol{\mathcal{R}}}(\underline{\gamma}) = \begin{bmatrix} \mathcal{R}_1(\underline{\gamma}) \\ \mathcal{R}_2(\underline{\gamma}) \\ \vdots \\ \mathcal{R}_{N_{\mathrm{slip}}}(\underline{\gamma}) \end{bmatrix}, \quad \underline{\gamma} = \begin{bmatrix} {}^{n+1}\gamma_1 \\ {}^{n+1}\gamma_2 \\ \vdots \\ {}^{n+1}\gamma_{N_{\mathrm{slip}}} \end{bmatrix}. \tag{3.34}$$

For an arbitrary Newton iteration k, we consider the system of equations

$$\left.\frac{\partial \underline{\boldsymbol{\mathcal{R}}}}{\partial \underline{\gamma}}\right|_{\underline{\gamma}^{(k)}} \Delta\underline{\gamma}^{(k)} = -\underline{\boldsymbol{\mathcal{R}}}\left(\underline{\gamma}^{(k)}\right). \tag{3.35}$$

The Newton update is then performed as

$$\underline{\boldsymbol{\gamma}}^{(k+1)} = \underline{\boldsymbol{\gamma}}^{(k)} + \Delta\underline{\boldsymbol{\gamma}}^{(k)} \tag{3.36}$$

where the increment $\Delta\underline{\boldsymbol{\gamma}}^{(k)}$ is obtained by solving (3.35). The updates continue until some convergence criterion is satisfied and $\underline{\boldsymbol{\gamma}}$ and hence $\{{}^{n+1}\gamma_\alpha\}_{\alpha=1}^{N_{\text{slip}}}$ are found. The automatic differentiation software Acegen REF is used to compute the Jacobian $\left.\dfrac{\partial\underline{\boldsymbol{\mathcal{R}}}}{\partial\underline{\boldsymbol{\gamma}}}\right|_{\underline{\boldsymbol{\gamma}}^{(k)}}$ in (3.35).

3.5.2 Global Structural Problem

In order to solve the finite element (global) problem using Newton's method, the Abaqus solver needs to assemble a global tangent stiffness matrix. This is achieved by using the algorithmic tangent stiffness tensor, often abbreviated as the ATS-tensor, which is given by

$$\frac{\mathrm{d}\boldsymbol{\sigma}}{\mathrm{d}\boldsymbol{\epsilon}} = \frac{\mathrm{d}\boldsymbol{\sigma}}{\mathrm{d}\Delta\boldsymbol{\epsilon}}. \tag{3.37}$$

To derive the ATS-tensor, we differentiate the expression for the updated stress $\boldsymbol{\sigma} = {}^{n+1}\boldsymbol{\sigma}$ in (3.32.1):

$$\frac{\mathrm{d}\boldsymbol{\sigma}}{\mathrm{d}\boldsymbol{\epsilon}} = \frac{\mathrm{d}\boldsymbol{\sigma}}{\mathrm{d}\Delta\boldsymbol{\epsilon}} = \frac{\mathrm{d}}{\mathrm{d}\Delta\boldsymbol{\epsilon}}\left[{}^{n}\boldsymbol{\sigma} + \boldsymbol{\mathcal{E}}^{\mathrm{e}} : (\Delta\boldsymbol{\epsilon} - \Delta\boldsymbol{\epsilon}^{\mathrm{p}})\right] = \boldsymbol{\mathcal{E}}^{\mathrm{e}} - \boldsymbol{\mathcal{E}}^{\mathrm{e}} : \frac{\mathrm{d}\Delta\boldsymbol{\epsilon}^{\mathrm{p}}}{\mathrm{d}\Delta\boldsymbol{\epsilon}}. \tag{3.38}$$

The next step is to differentiate $\Delta\boldsymbol{\epsilon}^{\mathrm{p}}$ in (3.32.2):

$$\frac{\mathrm{d}\Delta\boldsymbol{\epsilon}^{\mathrm{p}}}{\mathrm{d}\Delta\boldsymbol{\epsilon}} = \frac{\mathrm{d}}{\mathrm{d}\Delta\boldsymbol{\epsilon}}\left[\sum_{\alpha=1}^{N_{\text{slip}}} \Delta\gamma_\alpha \left(\mathbf{s}^\alpha \otimes \mathbf{m}^\alpha\right)^{\text{sym}}\right] = \sum_{\alpha=1}^{N_{\text{slip}}} \left(\mathbf{s}^\alpha \otimes \mathbf{m}^\alpha\right)^{\text{sym}} \otimes \frac{\mathrm{d}\Delta\gamma_\alpha}{\mathrm{d}\Delta\boldsymbol{\epsilon}} \tag{3.39}$$

The remaining unknown $\dfrac{\mathrm{d}\Delta\gamma_\alpha}{\mathrm{d}\Delta\boldsymbol{\epsilon}}$ which can be obtained by the fact that the local problem is satisfied for all $\Delta\epsilon$, i.e.

$$\mathcal{R}_\alpha(\{\Delta\gamma_\beta(\Delta\boldsymbol{\epsilon})\}, \Delta\boldsymbol{\epsilon}) = 0 \quad \forall\, \Delta\boldsymbol{\epsilon} \tag{3.40}$$

which gives that

$$\mathbf{0} = \frac{\mathrm{d}\mathcal{R}_\alpha}{\mathrm{d}\Delta\boldsymbol{\epsilon}} = \sum_{\beta=1}^{N_{\text{slip}}} \frac{\partial\mathcal{R}_\alpha}{\partial\gamma_\beta}\frac{\mathrm{d}\Delta\gamma_\beta}{\mathrm{d}\Delta\boldsymbol{\epsilon}} + \frac{\partial\mathcal{R}_\alpha}{\partial\Delta\boldsymbol{\epsilon}} \qquad \alpha = 1, 2, \ldots, N_{\text{slip}} \tag{3.41}$$

from which $\dfrac{\mathrm{d}\Delta\gamma_\alpha}{\mathrm{d}\Delta\boldsymbol{\epsilon}}$ can be solved for.

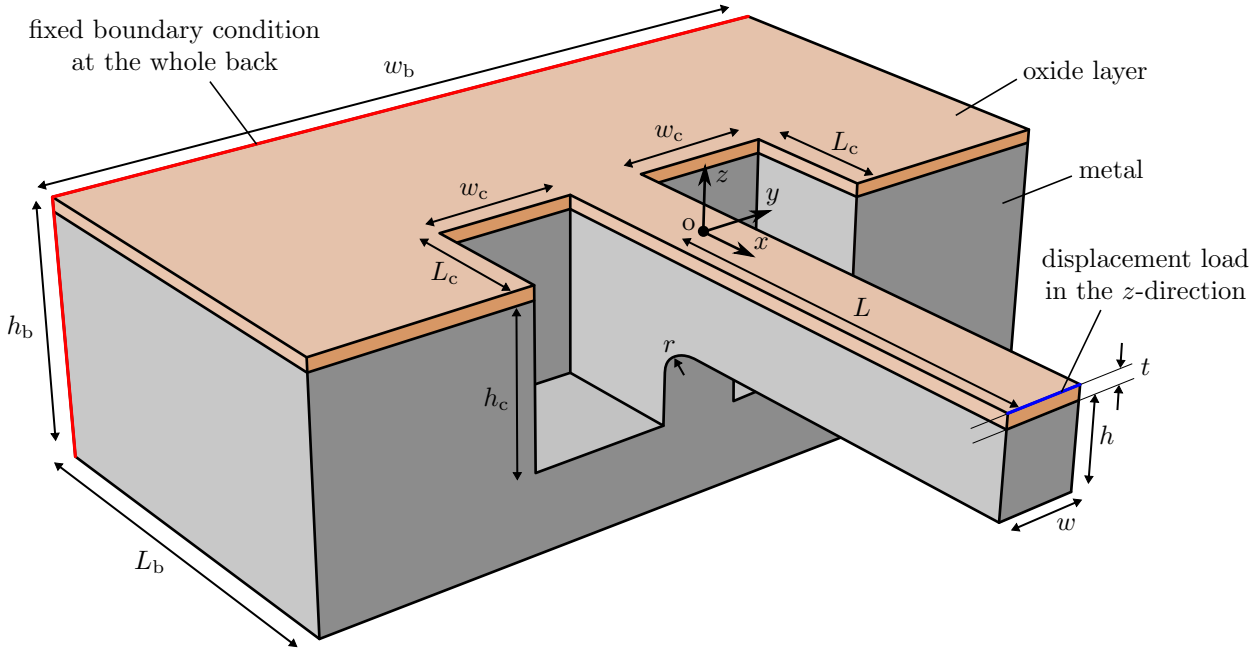

Figure 4.1: Illustration of the parametrized microbeam model. Material has been removed in the parts defined by geometry parameters L_c, h_c and w_c. This is done in order to get rid of stress concentrations that otherwise would occur in these regions.

4 Microbeam Finite Element Model

4.1 Parametrized Microbeam Model

In order simulate the microbeam bending experiments, a parametrized finite element microbeam model is developed in Abaqus CAE. As mentioned in the previous chapter, Abaqus is one of the commercial finite element programs that allows the (advanced) user to incorporate own material model subroutines into the analysis.

The microbeam model developed for the simulations is illustrated in Figure 4.1. As a boundary condition, the model is completely fixed at the whole back. Furthermore, the whole top edge of the microbeam is subjected to a displacement load in the z-direction. The modeling may be discussed comparing to the experiment setup illustrated in Figure 2.1. We could for instance choose to fix the bottom face of the structure as well. Regarding modeling of the diamond tip tool contact, a contact problem with a rigid body could be used. However, for this model we instead choose to prescribe the displacement of the whole top edge to decrease the model complexity. The force is then evaluated as the total reaction force from the equilibrium equations.

The block part at the back of the structure represents the rest of the material sample from which the microbeam is made. This part is described by the geometry parameters L_b, h_b, w_b, L_c, h_c and w_c. These parameters have no significant impact on the results and will be held constant for all simulations in this report at the values

$$L_b = 20\,\mu m, \quad h_b = 12\,\mu m, \quad w_b = 36\,\mu m, \quad L_c = 8\,\mu m, \quad h_c = 8\,\mu m, \quad w_c = 8\,\mu m.$$

The values of these parameters will not be repeated as we move on.

The model is set up using a Python script for Abaqus. The Python script is written to handle all of the most relevant model parameters including geometry, material parameters, boundary conditions and node set definitions. Using a script ensures that a consistent model setup is obtained. To systematically evaluate results like force-deflection data, postprocessing scripts are written as well. The reader can find more information about the Python scripts in Appendix A.

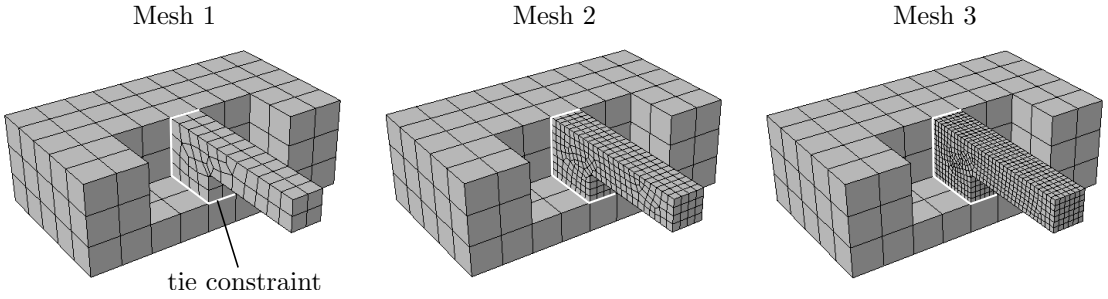

Figure 4.2: The three different meshes used in the element and convergence analysis. In each mesh, the microbeam part of the structure is connected to the rest using tie constraints between the surfaces.

4.2 Element and Convergence Analysis

In order to accurately predict the response of the microbeam, it is crucial to choose a suitable mesh and element type. Therefore, an element and convergence analysis is carried out to study the behavior of various elements and meshes. It is also important to take the total simulation time into consideration since very many simulations are expected to be needed in a numerical calibration task. The goal is to make a proper overall choice of mesh and element type to use for the microbeam bending simulations throughout this thesis.

Three different meshes will be investigated which all are illustrated in Figure 4.2. The elements included in the study are presented in Table 4.1. The naming of the elements follows the one used in Abaqus and its documentation. These are all three-dimensional continuum brick elements. Using a crystal plasticity constitutive model, it is preferred to use brick elements instead of tetrahedrons due to locking issues [4]. This is why no tetrahedron elements are included in the study.

Table 4.1: Abaqus continuum elements included in the study.

Element	Description
C3D8	8-node (linear) brick element, full integration.
C3D8R	8-node (linear) brick element, reduced integration, enhanced hourglass control.
C3D20	20-node (quadratic) brick element, full integration.
C3D20R	20-node (quadratic) brick element, reduced integration.

Fully integrated linear elements may result in a problem called shear locking when used in simulations of bending structures and modal analyses [10]. In order to avoid shear locking of linear elements, reduced integration can be used instead of a full one. On the other hand, reduced integration may result in another issue known as the hourglass effect in which spurious or zero-energy modes propagate among the elements. Abaqus includes a feature known as hourglass control where the user can add a stiffness associated with these zero-energy modes. In the case of the microbeam model, an hourglass control is needed when using the C3D8R element. The Abaqus setting "enhanced hourglass control" is used for the C3D8R element as stated in Table 4.1. Related to the discussion, it may also be mentioned that the Abaqus manual recommends quadratic elements for bending applications [9].

For the convergence and element analysis we introduce a microbeam with the dimensions

$$L = 15.0\,\mu\text{m}, \quad h = 4.0\,\mu\text{m}, \quad w = 4.0\,\mu\text{m}, \quad r = 0.4\,\mu\text{m}, \quad t = 0\,\mu\text{m (no oxide)}$$

and the crystal orientation described by the three Bunge angles

$$\varphi_1 = 302.3^\circ, \quad \Phi = 40.7^\circ, \quad \varphi_2 = 56.1^\circ.$$

The material parameters used are for the superalloy Inconel 718 which are given in Table 5.1. The convergence properties may be affected by some of the parameters, e.g. crystal orientation. However, in this study we choose to only consider one set of geometry and material parameters.

Convergence analysis results are presented in Table 4.2 for four different deflection points. These simulations are run with constant tolerances for the Newton iterations which is not the default setting in Abaqus. Simulation run times are presented as well to compare the computational cost. All simulations are performed on a local desktop computer using parallelization mode in Abaqus with four CPU:s.

Table 4.2: Convergence analysis results in terms of reaction force (µN) for different elements and meshes. Data is presented for four deflections where 0.5 µm can be used to compare elastic responses. Run times are presented for simulations using four CPU:s on a local desktop computer. The first term in this column refer to simulation time whereas the second term is the time spent on postprocessing.

		0.5 µm	1.0 µm	3.0 µm	5.0 µm	Simulation time
C3D8	Mesh 1	838.87	1384.60	1948.15	2120.41	68 s + 16 s
	Mesh 2	775.06	1232.32	1690.35	1861.38	147 s + 25 s
	Mesh 3	762.70	1200.90	1617.31	1774.81	330 s + 25 s
C3D8R	Mesh 1	819.37	1402.29	2332.86	2901.85	55 s + 12 s
	Mesh 2	774.97	1258.47	1818.25	2131.83	72 s + 15 s
	Mesh 3	767.86	1219.92	1704.73	1943.93	125 s + 17 s
C3D20	Mesh 1	754.66	1183.32	1585.77	1745.64	167 s + 40 s
	Mesh 2	741.33	1162.87	1540.15	1682.09	470 s + 350 s
	Mesh 3	734.98	1152.61	1524.24	1659.78	1303 s + 740 s
C3D20R	Mesh 1	746.86	1168.66	1550.03	1679.68	90 s + 13 s
	Mesh 2	736.69	1153.41	1528.53	1658.84	223 s + 15 s
	Mesh 3	730.57	1149.06	1512.08	1593.22	3755 s + 240 s

The linear element types C3D8 and C3D8R both show inferior convergence properties compared to C3D20 and C3D20R. Since element types C3D20 and C3D20R have more degrees of freedom, one can argue that this is not a fair comparison. As expected, with a constant number of elements, simulation times are increased for C3D20 and C3D20R as compared to C3D8 and C3D8R. However, the differences in simulation time for mesh 1 are not great. This may partly be due to constant overhead routines setting up each one of the analyses, for example linking the user subroutine.

Some of the force-deflection plots corresponding to the rows in Table 4.2 are plotted in Figure 4.3. Response curves for C3D20 and C3D20R with mesh 3 are expected to be the most accurate ones. Comparing responses for mesh 1, element type C3D20R seem to be the best performer. It is noted in the figure that using element type C3D8 or C3D8R results in locking. The hourglass control for C3D8R clearly results in an overly stiff response. Also, note the peculiar drop in force for element type C3D20R with mesh 3 around the deflection 4.20 µm. Very many iterations take place here which explains the long simulation time. This behavior has been observed for crystal plasticity constitutive models in other papers as well, see for example Reference [11]. However, this behavior will not be investigated further in this report.

When performing a calibration task we want to keep the simulation run times short but still work with accurate results from the finite element analyses. A reasonable criterion is that we could spend a maximum of 2 to 3 minutes on a single simulation together with postprocessing. Since the calibration is intended to be run on a local computer, the simulation times in Table 4.2 are good guidelines. Based on the result from the convergence study as well as the time requirement, we choose element type C3D20R and mesh 1.

4.3 Example Simulations

To further test the parametrized microbeam model, we will now look at a study of the oxide layer influence on the force-deflection response. The chosen microbeam geometry measures are

$$L = 15.0\,\mu\text{m}, \quad h = 4.0\,\mu\text{m} - t, \quad w = 4.0\,\mu\text{m}, \quad r = 0.4\,\mu\text{m}$$

where t is the thickness of the oxide layer. This means that the total height of the beam cross section is constant. The crystal orientation is again described by the Bunge angles

$$\varphi_1 = 302.3^\circ, \quad \Phi = 40.7^\circ, \quad \varphi_2 = 56.1^\circ.$$

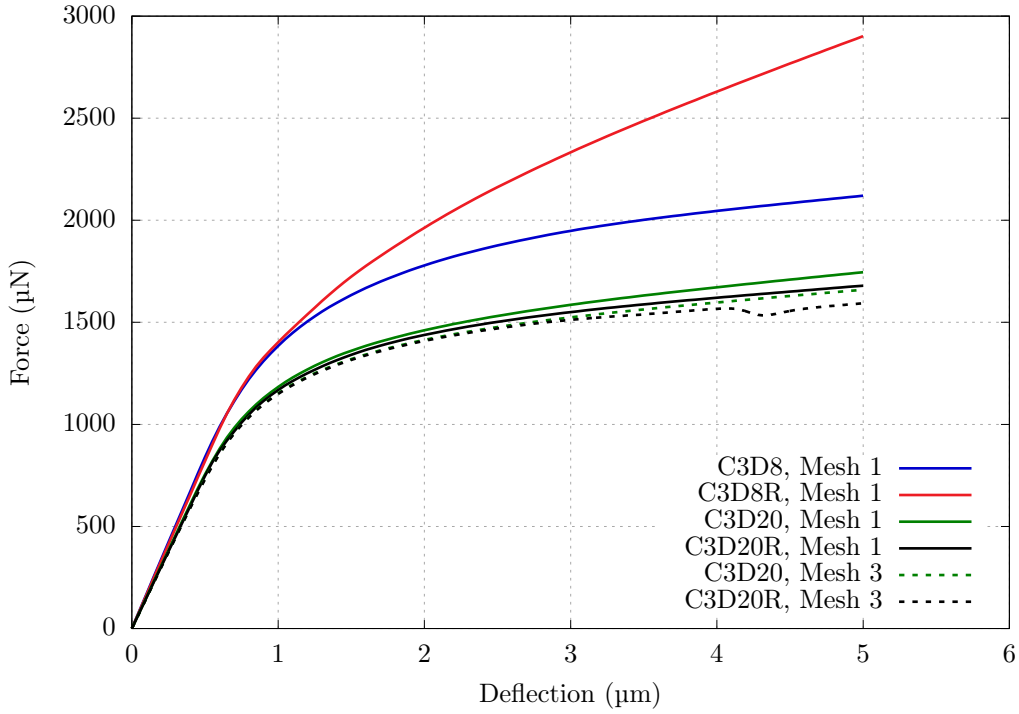

Figure 4.3: Some of the force-deflection curves obtained in the convergence analysis.

Also, the crystal plasticity material parameters are again chosen as the Inconel 718 numbers in Table 5.1. The oxide is assumed to be isotropically linear elastic with Young's modulus set to 275 GPa and Poisson's ratio at 0.25.

The force-deflection responses are plotted in Figure 4.4 for $t = 0\,\text{nm}$, $50\,\text{nm}$, $100\,\text{nm}$, $200\,\text{nm}$ and $400\,\text{nm}$. It is clear that increased oxide layer thickness results in a stiffer response. This can be expected since it is only the crystal orientations with Miller index direction around [1 1 1] along the microbeam that can compete with the high Young's modulus of oxide, cf. Figure 3.2. Also, the oxide is not modeled with any plasticity features.

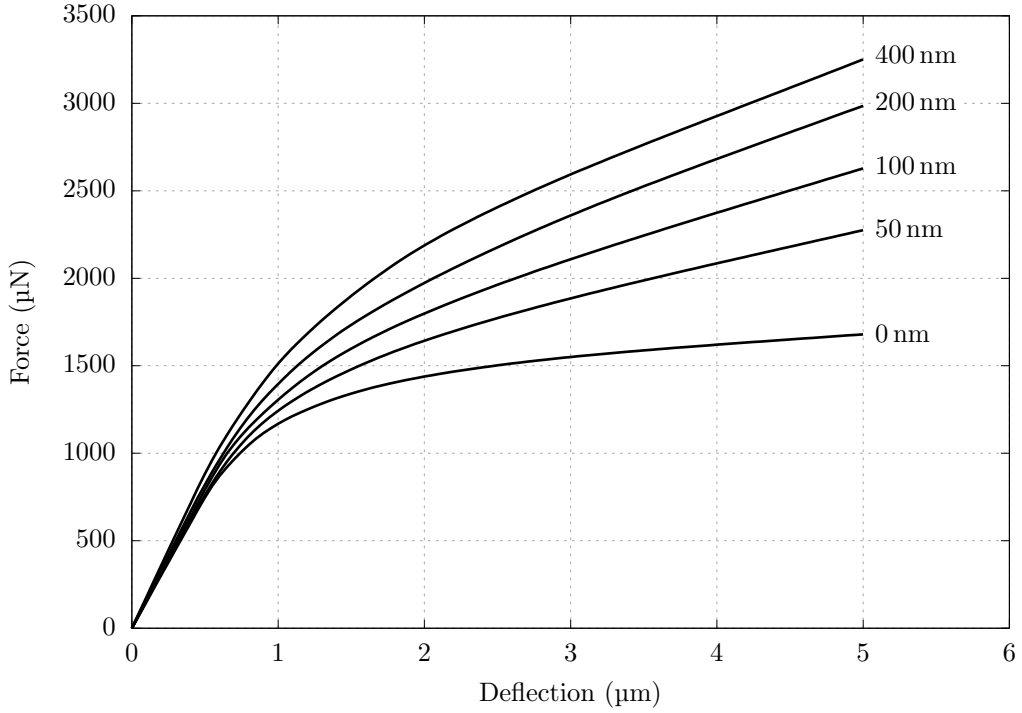

Figure 4.4: Study of oxide layer influence on the force-deflection response. The total height (i.e. crystal and oxide) of the beam cross section is constant for all simulations.

5 Calibration of Crystal Plasticity Model

This chapter covers calibration of the crystal plasticity model presented in Chapter 3 using finite element simulations featuring the microbeam model from Chapter 4. The mathematical formulation of the calibration procedure is presented in the chapter's first section. In Section 5.2, a "fictitious" calibration is performed. This calibration is based on results from finite element simulations for a set of known material parameter values. These parameters are then slightly disturbed as an initial guess and then calibrated to fit the force-deflection fictitious data. If the problem has a unique solution, the known material parameter values used to produce the fictitious data are hopefully found.

Calibration based on real microbeam bending experiment data is presented in Section 5.3. This calibration features the successful experiment with microbeam B that was introduced in Chapter 2. A visual comparison between the slip lines obtained in all three experiments and the most active slip systems in the finite element simulations is also presented and discussed.

Suggested parameter values for the superalloy Inconel 718 using the chosen crystal plasticity model are presented in Table 5.1. These were calibrated using data from micropillar compression experiments, see Reference [8]. Since Inconel 718 and Allvac 718 Plus are similar, these numbers will be used as guidelines for Allvac 718 Plus. In particular, these parameters will be used to obtain data for the fictitious calibration.

Table 5.1: Crystal plasticity parameter values for Inconel 718 from Reference [8].

Inconel 718										
Elastic parameters			Plastic parameters							
1	2	3	4	5	6	7	8	9	10	11
C_{11}	C_{12}	C_{44}	$\dot{\gamma}_0$	m	h_∞	h_0	τ_∞	τ_0	$q_{\alpha\alpha}$	$q_{\alpha\beta}$
GPa	GPa	GPa	1/s	–	GPa	GPa	MPa	MPa	–	–
259.6	179.0	109.6	0.10	0.017	0.3	6.0	598.5	465.5	1.0	1.0

5.1 Mathematical Formulation

The task of calibrating material parameters can be formulated mathematically as an optimization problem. In optimization problems, one searches for a solution that either minimizes or maximizes an objective function. In our case of microbeam bending, we have force-deflection response data that we try to fit by the means of altering the values of all or some of the material parameters. Let us denote the numerical values of these parameters by $p = (p_1, p_2, \ldots, p_m)$. The objective function should, in some sense, quantify the deviation of the current model response (function of p) from the experimental data.

Since the experimental data and the simulation data in general are obtained for different deflection points, the approach taken here is to first linearly interpolate both the experimental data and the model response. The force level in n deflection points $\{\delta_i\}_{i=1}^n$ are then evaluated such that two sets of points are obtained: $\{(\delta_i, F_{\text{exp},i})\}_{i=1}^n$ and $\{(\delta_i, F_{\text{sim},i}(p))\}_{i=1}^n$. The subscript "exp" refers to the experimental data and "sim" refers to simulation. The objective function is then conveniently chosen in a least-squares manner as

$$f(p) = \sqrt{\sum_{i=1}^{n} \left(F_{\text{exp},i} - F_{\text{sim},i}(p)\right)^2}\,. \tag{5.1}$$

There are some issues that are worth mentioning. Since the material model shows time-dependency, it is preferred that both the experiment and the simulation are considered for the same load rate. This could be an issue dealing with experimental data of varying load rate. Also, if data including unloading or cyclic loading is to be interpolated, time might be a more suitable independent variable for the interpolation as compared to deflection.

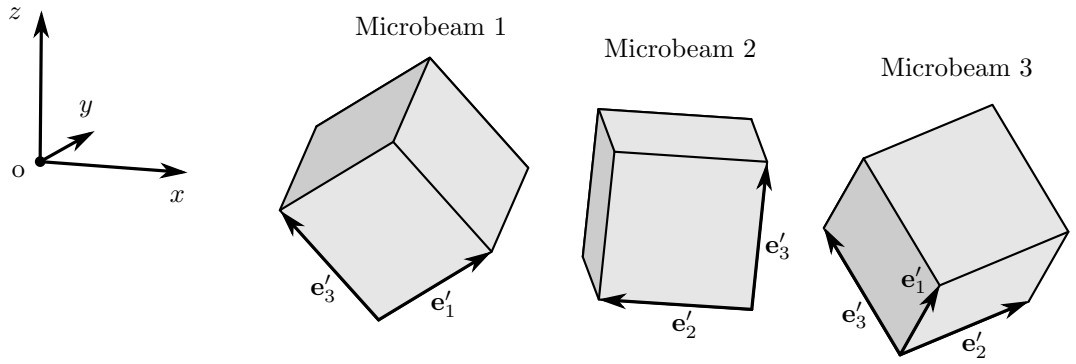

Figure 5.1: Illustration of the crystal orientations for microbeam 1, 2 and 3 in Table 5.2. The coordinate system oxyz is consistent with the experiment illustration in Figure 2.1 which means that the microbeam is aligned along the x-axis.

5.2 Calibration Based on Fictitious Data

A fictitious calibration is first performed using "experimental data" from finite element simulations. The term "fictitious" is used to clearly distinguish this activity from a calibration involving real experimental data. This is a way to not only explore the features of the constitutive model, but also to discover possible caveats or pitfalls related to its calibration. Examples of issues that can arise is lack of sensitivity for certain material parameters or multiple solution sets for the optimization problem. There is also a possibility that some parameters need to be constrained relative to each other.

Three microbeams which are called 1, 2 and 3 are chosen for the fictitious calibration. These three microbeams all have the same geometry but different crystal orientations compared to each other. Geometry and orientation of the microbeams are presented in Table 5.2. The crystal orientation for microbeam 1, 2 and 3 are chosen to be the same as for the experiment microbeams A, B and C, respectively. An illustration of these three crystal orientations is given in Figure 5.1.

Since microbeams 1, 2 and 3 all have the same geometry, it means that the same mesh can be used for the simulations of these microbeams. The chosen mesh is illustrated in Figure 5.2. Using the initial material parameters of Inconel 718 in Table 5.1, the force-deflection curves obtained for these microbeams are plotted in Figure 5.3. The deflection loading rate used is 0.05 µm/s. This means that the maximum and final deflection of 5 µm is obtained after a total time of 100 s. This loading rate is used for all simulations throughout this chapter. The data plotted in Figure 5.3 will serve as the "experimental data" for the fictitious calibration.

The fictitious calibration problem is split up into two parts. First, a calibration of the elastic parameters C_{11}, C_{12} and C_{44} is performed. Once the elastic problem is solved for, a calibration of the plastic parameters h_∞, h_0, τ_∞ and τ_0 is considered. The four plastic parameters $\dot{\gamma}_0$, m, $q_{\alpha\alpha}$ and $q_{\alpha\beta}$ are left out of the calibration. This decision will also drastically reduce the calibration space and hence the computational effort. The four omitted parameters are held fixed at the suggested Inconel 718 numbers in Table 5.1. However, the influences of parameters $q_{\alpha\alpha}$ and $q_{\alpha\beta}$ will be studied in Subsection 5.2.3.

Table 5.2: Geometries and crystal orientations for the fictitious microbeams.

Fictitious microbeams							
Beam	Geometry				Orientation		
	L (µm)	w (µm)	h (µm)	r (µm)	φ_1	Φ	φ_2
1	15.0	4.0	4.0	0.4	302.3°	40.7°	56.1°
2	15.0	4.0	4.0	0.4	79.3°	6.8°	36.9°
3	15.0	4.0	4.0	0.4	247.4°	41.9°	68.1°

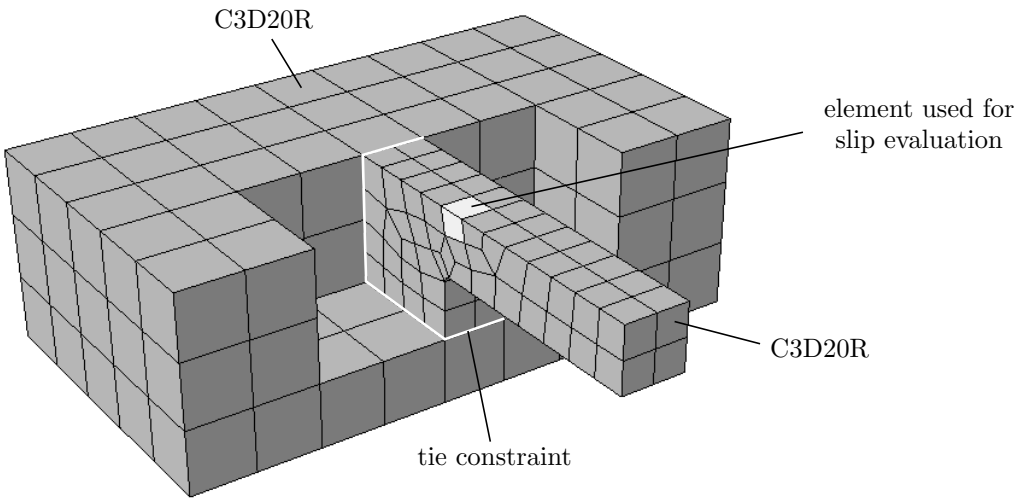

Figure 5.2: Mesh used for simulations of microbeams 1, 2 and 3. Designation C3D20R refers to the Abaqus element type used (three-dimensional continuum element with reduced integration). Since this is a rather coarse mesh, mesh refinements become cumbersome. A tie constraint is therefore used to connect the microbeam part (finer elements) to the rest of the structure (coarser elements).

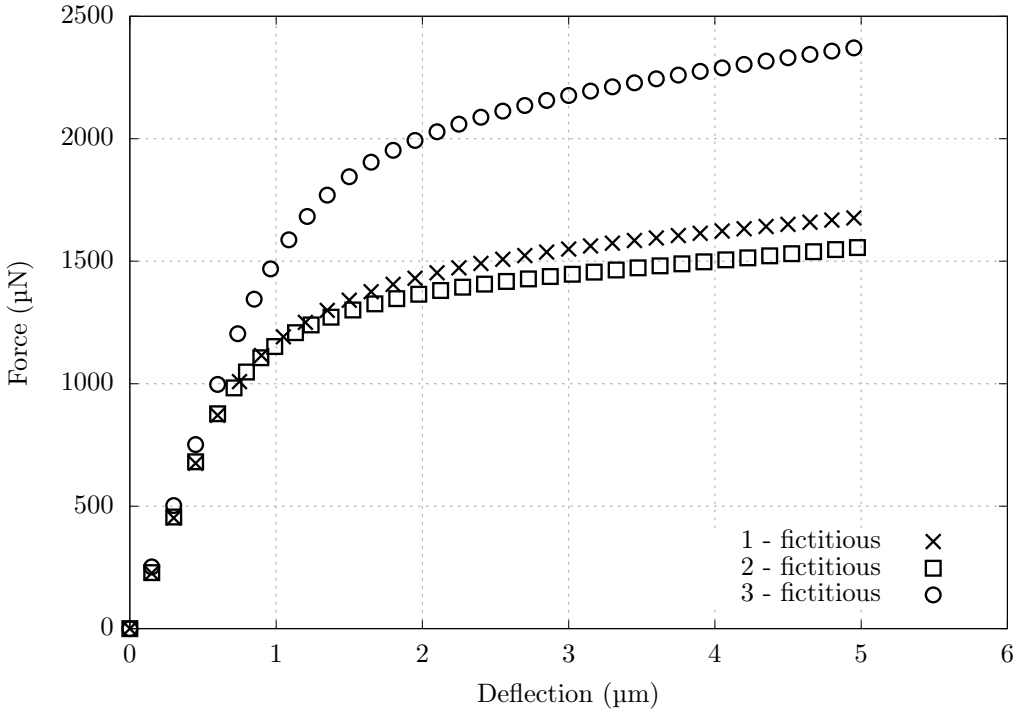

Figure 5.3: Force-deflection plots for microbeams 1, 2 and 3 of Table 5.2 using the parameter values in Table 5.1. This data will serve as "experimental data" for the fictitious calibration.

5.2.1 Finding Elastic Parameters C_{11}, C_{12} and C_{44}

For the calibration of the elastic response, we consider the problem of finding the correct combination or combinations of parameters C_{11}, C_{12} and C_{44}. Any solution should give the objective elastic beam stiffnesses for each one of the three fictitious microbeams. The stiffness quantity can be interpreted as the slope of the elastic loading part in a force-deflection response curve and will be denoted k or F/δ. The F/δ-stiffnesses can also be altered by the means of changing geometry and/or crystal orientation. However, the geometry and orientation are known for each microbeam and therefore held fixed.

The F/δ-stiffness for the fictitious microbeams 1, 2 and 3 will be denoted k_1, k_2 and k_3, respectively. The corresponding "experimental results" can be evaluated from the responses in Figure 5.3 and are given by

$$k_{1,\text{fictitious}} = 1495.31\,\text{N/m}, \quad k_{2,\text{fictitious}} = 1504.30\,\text{N/m}, \quad k_{3,\text{fictitious}} = 1662.05\,\text{N/m}. \tag{5.2}$$

Let us introduce the optimization variables s_1, s_2 and s_3 defining the elastic parameters C_{11}, C_{12} and C_{44}, respectively. These variables will simply scale the reference values of Inconel 718 such that

$$C_{11}(s_1) = s_1 C_{11,\text{IN718}}, \quad C_{12}(s_2) = s_2 C_{12,\text{IN718}}, \quad C_{44}(s_3) = s_3 C_{44,\text{IN718}} \tag{5.3}$$

where subscript "IN718" refers to the corresponding parameter value in Table 5.1. Defining the optimization variables like this is mostly a matter of convenience. However, if the optimization variables are of the same order, it is also easier to define optimization tolerances.

Now, the three microbeam stiffnesses k_1, k_2 and k_3 are considered to be functions of s_1, s_2 and s_3. We want to find any combination (s_1, s_2, s_3) that solves system of equations

$$\begin{cases} k_1(s_1, s_2, s_3) = k_{1,\text{fictitious}} = 1495.31\,\text{N/m}, \\ k_2(s_1, s_2, s_3) = k_{2,\text{fictitious}} = 1504.30\,\text{N/m}, \\ k_3(s_1, s_2, s_3) = k_{3,\text{fictitious}} = 1662.05\,\text{N/m}. \end{cases} \tag{5.4}$$

We known that at least $(s_1, s_2, s_3) = (1, 1, 1)$ is a solution since these variables were used to generate the "experimental data".

The numerical solution to each one of the equations in (5.4) is plotted in Figure 5.4. These surfaces are obtained from an individual optimization of the variable s_3 for 5×5 grid points in the $s_1 s_2$-plane. Although not entirely evident from the plot itself, an approximate solution is obtained along a curve where all three surfaces intersect. Hence, the numerical problem seems to have multiple solutions and it will not be possible to uniquely find the elastic parameters.

It is noted that the solution surfaces for microbeam 1 and 2 are very close to each other in Figure 5.4. The intersection of surfaces for microbeams 1 and 2 will then be very sensitive to variations. Hence, orientations of microbeams 1 and 2 alone are not particularly good choices to solve the problem if real experimental data were to be used. On the other hand, physical experiments with these orientations could be useful for verification purposes. Furthermore, as can be seen in Figure 5.3, the plastic response characteristics may differ. In this regard, these orientations may provide valuable information.

To summarize, we need to introduce some additional constraint if C_{11}, C_{12} and C_{44} should be determined altogether. One possibility is to make use of the Zener ratio which characterizes the degree of anisotropy of cubic crystals [12]. The formula for the Zener ratio a_r is given by

$$a_\text{r} = \frac{2\,C_{44}}{C_{11} - C_{12}} \tag{5.5}$$

where $a_\text{r} = 1$ corresponds to an isotropic crystal. Interpreted in terms of the Zener index, it is possible to find a solution if the degree of anisotropy is provided. This suggests that is might be possible to find a unique solution by taking a multiaxial response of the microbeam bending into account when calibrating the elastic parameters.

Proceeding to the calibration of the plastic parameters in the next subsection, we set C_{11}, C_{12} and C_{44} to the Inconel 718 reference values in Table 5.1, i.e. using $(s_1, s_2, s_3) = (1, 1, 1)$.

5.2.2 Finding Plastic Parameters h_∞, h_0, τ_∞ and τ_0

For calibration purposes of plastic parameters based on the fictitious data, we will limit ourselves to study h_∞, h_0, τ_∞ and τ_0 as already mentioned. The effect obtained by varying $q_{\alpha\alpha}$ and $q_{\alpha\beta}$ will be covered in the next subsection.

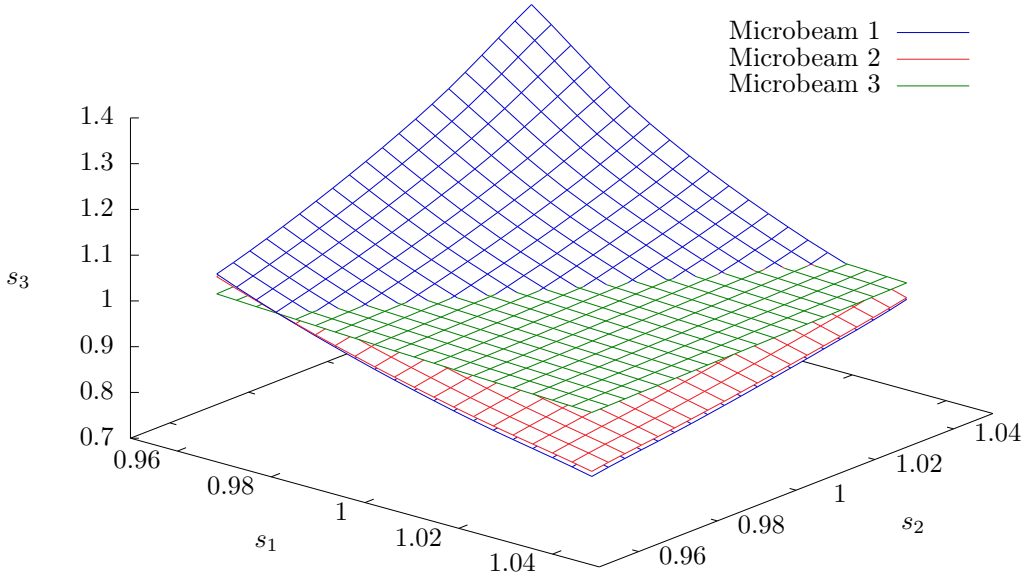

Figure 5.4: Surfaces for the elastic parameter combinations that results in correct F/δ-stiffness for each one of the fictitious microbeams 1, 2 and 3.

In the same way as for the elastic parameters, the optimization variables s_6, s_7, s_8 and s_9 are now introduced for h_∞, h_0, τ_∞ and τ_0:

$$h_\infty(s_6) = s_6 h_{\infty,\text{IN718}}, \quad h_0(s_7) = s_7 h_{0,\text{IN718}}, \quad \tau_\infty(s_8) = s_8 \tau_{\infty,\text{IN718}}, \quad \tau_0(s_9) = s_9 \tau_{0,\text{IN718}}. \tag{5.6}$$

As before, the constants subscripted with "IN718" refer to the Inconel 718 parameter values in Table 5.1. Also, a constraint is added concerning s_8 and s_9 to ensure that $\tau_\infty \geq \tau_0$. Without this constraint, the model behavior may become strange. Abrupt model behavior changes may be harmful when dealing with numerical optimization algorithms.

The parameters (s_6, s_7, s_8, s_9) are now disturbed from $(1, 1, 1, 1)$. The goal is to calibrate the parameters such that the original responses in Figure 5.3 are found again. An optimization is performed using a Nelder-Mead (also called simplex) method in Matlab. Details about how the Abaqus simulations are called iteratively from Matlab with updated material parameters are presented in Appendix B. The initial guesses for the optimization variables are chosen as

$$s_6^{(0)} = 0.90, \quad s_7^{(0)} = 1.10, \quad s_8^{(0)} = 1.10, \quad s_9^{(0)} = 0.90. \tag{5.7}$$

Force-deflection plots for these initial guesses may be compared with the "experimental data" in Figure 5.5.

The evolution history of the optimization variables when calibrating are plotted in Figure 5.6. The optimization is terminated with satisfying responses at the values

$$s_6^{(\text{final})} = 1.0286, \quad s_7^{(\text{final})} = 1.0582, \quad s_8^{(\text{final})} = 0.9973, \quad s_9^{(\text{final})} = 0.9952.$$

Force-deflection plots with these parameter values are given in Figure 5.5. At this point, variables s_8 and s_9 (which determine τ_∞ and τ_0, respectively) both seem to have found an optimal level close to 1. However, there seem to be lower sensitivities for variables s_6 and s_7 (determining h_∞ and h_0). These parameters are still subjected to changes at the point of termination although the agreement with "experimental data" in Figure 5.5 is very good.

One might suspect that the fictitious plastic optimization problem has a unique solution which means that (s_6, s_7, s_8, s_9) will approach $(1, 1, 1, 1)$ if the calibration would be continued. However, variables s_6 and s_7 require greater changes to impact the force-deflection curves than s_8 and s_9. Hence, s_6 and s_7 could have been disturbed more for their initial guess.

5.2.3 Parameters $q_{\alpha\alpha}$ and $q_{\alpha\beta}$

The hardening parameters $q_{\alpha\alpha}$ and $q_{\alpha\beta}$ are interesting since these, loosely speaking, control the hardening distribution among slip systems. Parameter $q_{\alpha\alpha}$ is often referred to as self-hardening whereas $q_{\alpha\beta}$ is called

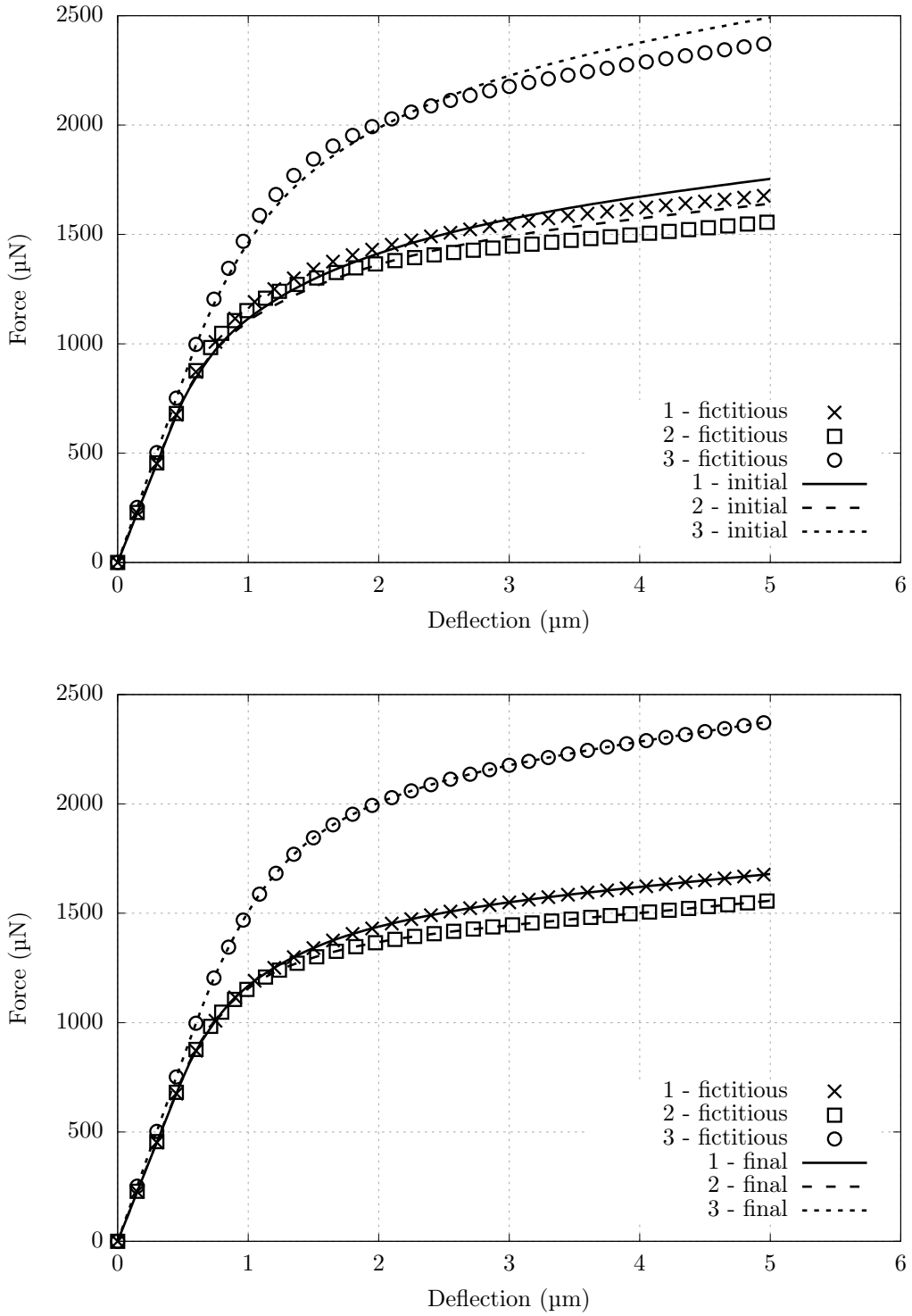

Figure 5.5: Initial and final response for the fictitious calibration of plastic parameters h_0, h_∞, τ_0 and τ_∞.

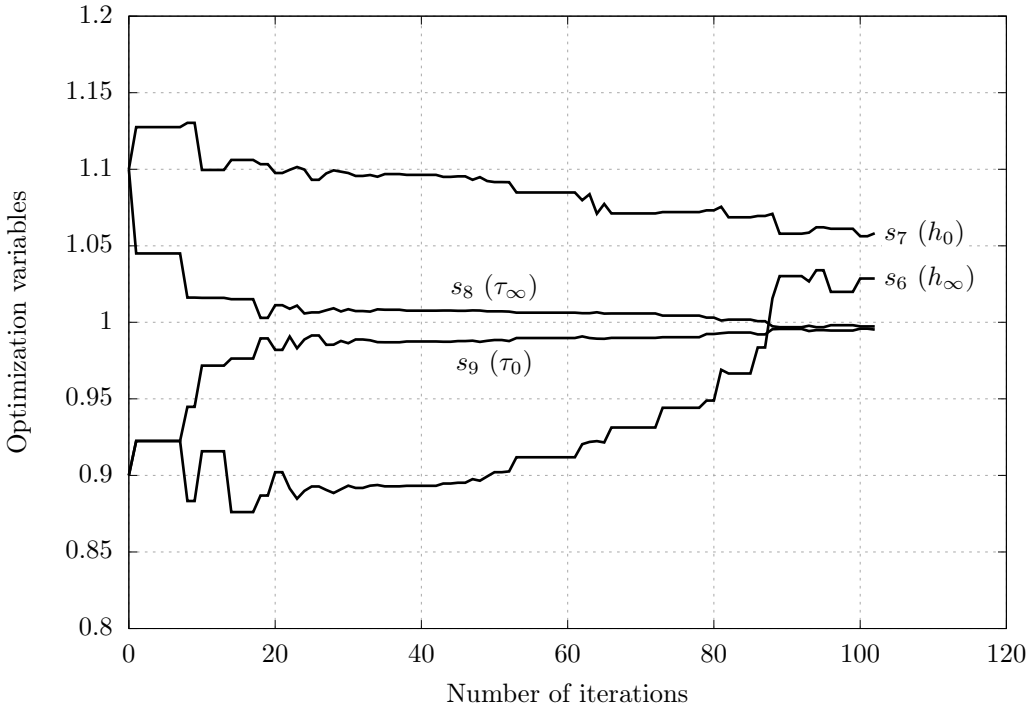

Figure 5.6: Evolution of optimization variables s_6, s_7, s_8 and s_9 for the fictitious calibration of the plastic parameters h_∞, h_0, τ_∞ and τ_0. The Nelder-Mead method, also known as a simplex method was used for the optimization through Matlab's built-in function `fminsearch`. More information about the calibration programming can be found in Appendix B.

latent- or cross-hardening.

We will now turn to a parametric study of material parameters $q_{\alpha\alpha}$ and $q_{\alpha\beta}$ using fictitious microbeam 1 in Table 5.2. Plots for evolution of slip variables γ_1 to γ_{12} for three different combinations of $q_{\alpha\alpha}$ and $q_{\alpha\beta}$ are plotted in Figure 5.7. The numbering of the slip variables γ_1 to γ_{12} refers to the numbering of the slip systems in Table 3.1. The slip of each system is evaluated for the centroid of the highlighted element in Figure 5.2 for which significant slip is obtained. Besides varying $q_{\alpha\alpha}$ and $q_{\alpha\beta}$, the other parameters are set to the Inconel 718 reference values in Table 5.1.

Slip system 10 shows dominant slip in all plots of Figure 5.7 and may be referred to as the primary slip system. For the parameter values $(q_{\alpha\alpha}, q_{\alpha\beta}) = (1, 1)$ in the first plot, we also obtain significant slip in system 4. Now, if the self-hardening parameter $q_{\alpha\alpha}$ is increased to 2 while $q_{\alpha\beta}$ is kept at 1, we obtain the evolution in the second plot. Increased self-hardening will decrease the primary slip of γ_{10} and increase the other ones, especially notable for γ_4 in this case. If instead the cross-hardening $q_{\alpha\beta}$ is increased to 2 while keeping $q_{\alpha\alpha} = 1$, the third plot is obtained. It is noted that slip system 4 now becomes insignificant due to the high cross-hardening.

Force-deflection curves for the three $(q_{\alpha\alpha}, q_{\alpha\beta})$ -combinations are plotted in Figure 5.8. The changes in responses obtained by varying the values of $q_{\alpha\alpha}$ and $q_{\alpha\beta}$ are similar to what can be achieved by changing other parameters. Hence, without detailed knowledge of how the slip is distributed among the slip systems, it is hard to calibrate $q_{\alpha\alpha}$ and $q_{\alpha\beta}$. This is why these parameters are held constant and not are calibrated here.

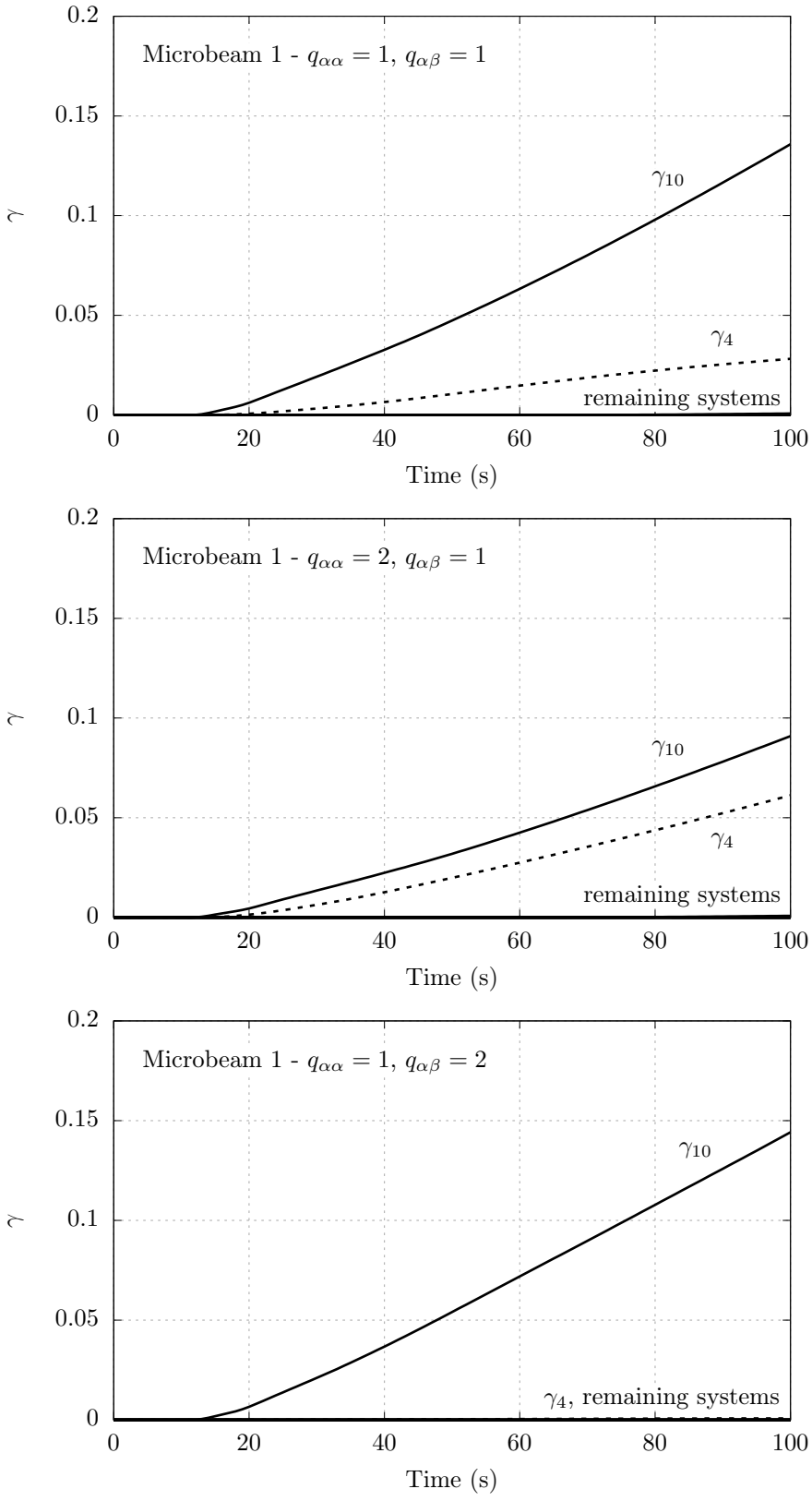

Figure 5.7: Evolution of slip variables γ_1 to γ_{12} for three different combinations of $q_{\alpha\alpha}$ and $q_{\alpha\beta}$. The subscript of the slip variables refer to slip systems in Table 3.1. Simulations are for microbeam 1 with the rest of the parameters set to Inconel 718 values in Table 5.1.

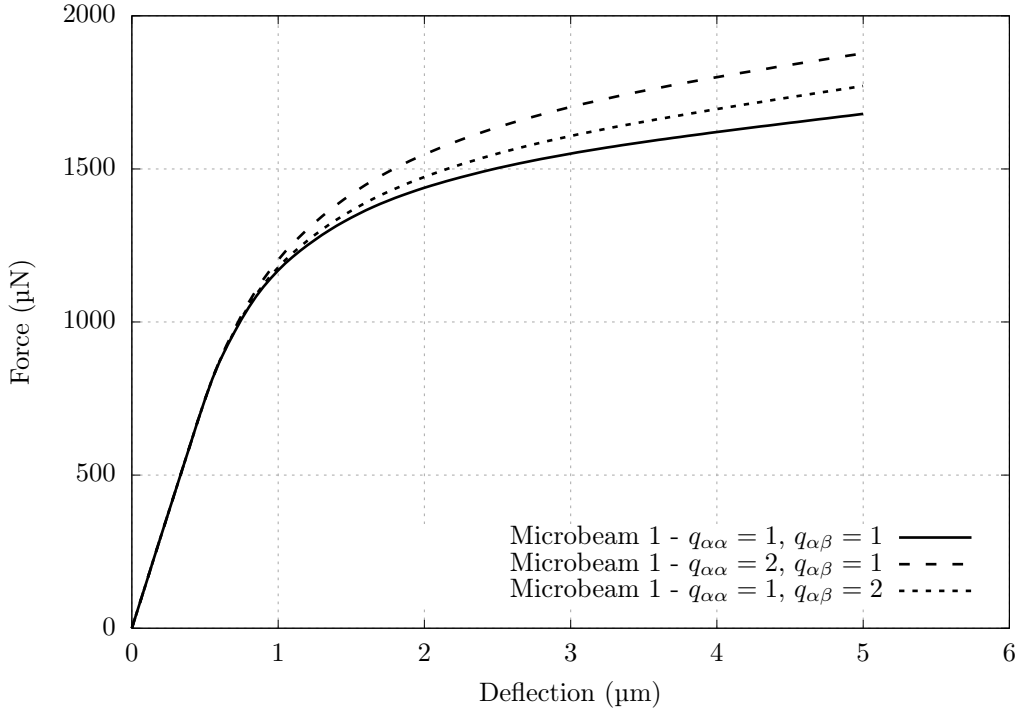

Figure 5.8: Parametric study for different combinations of $(q_{\alpha\alpha}, q_{\alpha\beta})$ for microbeam 1 with the rest of the parameters set to Inconel 718 reference values in Table 5.1.

5.3 Calibration Based on Experimental Data

We now turn to a calibration based on experimental data from the microbeam bending experiments described in Chapter 2. The geometries and orientations of the three experiment microbeams A, B and C are presented again in Table 5.3. Also, recall that the experiments using microbeam A and C unfortunately failed. The force-deflection data for the successful microbeam B experiment is plotted in Figure 5.9.

The calibration based on experimental data follows the same pattern as the calibration based on the fictitious experiments. In other words, first the elastic parameters C_{11}, C_{12} and C_{44} are calibrated and then the plastic parameters h_∞, h_0, τ_∞ and τ_0. However, now we only have one experimental response (experiment data for microbeam B) as compared to three "experiment" responses for the fictitious calibration. A comparison between the activated slip systems in the simulations and the obtained slip lines from experiment images is also performed for verification purposes.

Since the geometry of the experiment microbeams A, B, C are not the same, different meshes need to be used for these microbeams. The chosen meshes are illustrated in Figure 5.10. The elements that are highlighted are used for slip system verification in Subsection 5.3.3.

In Figure 5.11, finite element model responses for microbeams A, B and C are plotted using the Inconel 718 parameters in Table 5.1. The crystal orientations for A, B and C are the same as for the fictitious microbeams 1, 2 and 3, respectively. However, comparing Figure 5.3 to Figure 5.11 it may be noted that the beam stiffnesses are greatly affected by the differences in geometry.

Table 5.3: Geometries and crystal orientations for the microbeams used in the experiments. These microbeams are made of the Allvac 718 Plus superalloy.

	Experiment microbeams						
Beam	Geometry				Orientation		
	L (µm)	w (µm)	h (µm)	r (µm)	φ_1	Φ	φ_2
A	10.45	4.2 ± 0.04	3.6 ± 0.03	0.4	302.3°	40.7°	56.1°
B	13.0	3.0 ± 0.06	3.9 ± 0.04	0.11	79.3°	6.8°	36.9°
C	11.8	4.0 ± 0.04	3.8 ± 0.06	0.35	247.4°	41.9°	68.1°

5.3.1 Finding Elastic Parameters C_{11}, C_{12} and C_{44}

As before, the problem of determining elastic parameters C_{11}, C_{12} and C_{44} that results in the correct F/δ-stiffness yields a surface of solutions. From the experimental data for microbeam B in Figure 5.9, the F/δ-stiffness is estimated to about 2000 N/m. However, with only a single microbeam, the one denoted B, we need two scalar constraints in order to uniquely determine C_{11}, C_{12} and C_{44}. We can now realize that it will not be possible to find accurate elastic parameters with this experimental data. However, we still may be able to draw useful conclusions from the results.

We introduce s_1, s_2 and s_3 as in the fictitious calibration, see Equation (5.3). For the first constraint, we somewhat arbitrarily pick $s_1 = 1.25$ because the microbeam stiffness needs to be drastically increased from the Inconel 718 parameters to fit the data. As the second constraint we may assume that Allvac 718 Plus has the same Zener index a_r as Inconel 718, i.e. $a_\mathrm{r} = 2.71$. Imposing these constraints, the solution is obtained as $(s_1, s_2, s_3) = (1.250, 1.184, 1.405)$ or

$$C_{11} = 324.5\,\mathrm{GPa}, \quad C_{12} = 211.8\,\mathrm{GPa}, \quad C_{44} = 154.0\,\mathrm{GPa}. \tag{5.8}$$

These values seem very high and inaccurate since the elastic parameters for Allvac 718 Plus are expected to be about the same as for the Inconel 718. The results will be discussed further in Chapter 6.

5.3.2 Finding Plastic Parameters h_∞, h_0, τ_∞ and τ_0

With the elastic response calibrated, suitable plastic parameter values for h_∞, h_0, τ_∞ and τ_0 are now to be found. The concept of optimization variables s_6, s_7, s_8 and s_9 are used again as in Equation (5.6). Using the Nelder-Mead method, the evolution of the optimization variables are plotted in Figure 5.12. The final values

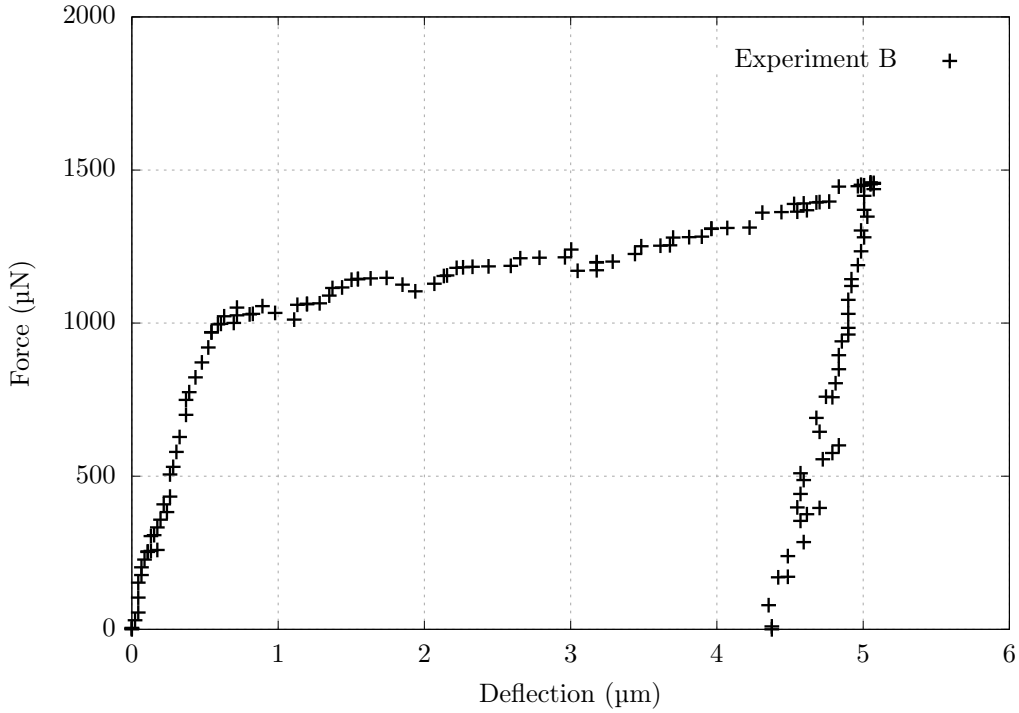

Figure 5.9: Force-deflection data from the successful experiment with microbeam B. Images from which the data is evaluated were acquired once per second. The total time elapsed up to the point of unloading is approximately 100 seconds.

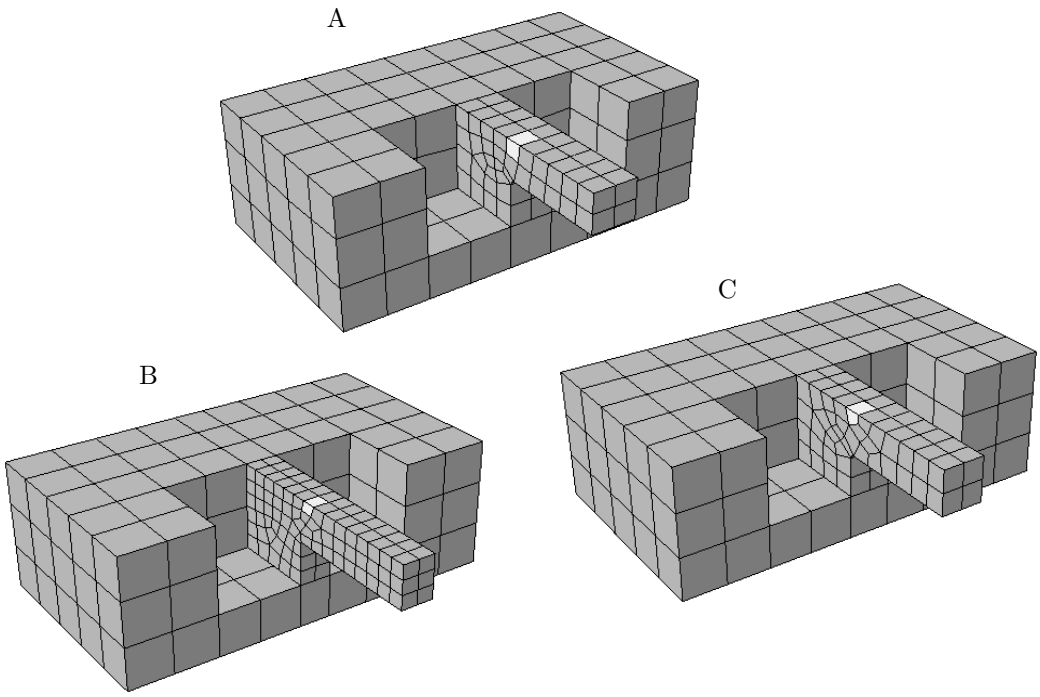

Figure 5.10: Meshes used for simulations of microbeams A, B and C. All elements are of the type C3D20R. The highlighted elements are used to evaluate slip for the slip lines verification in Subsection 5.3.3.

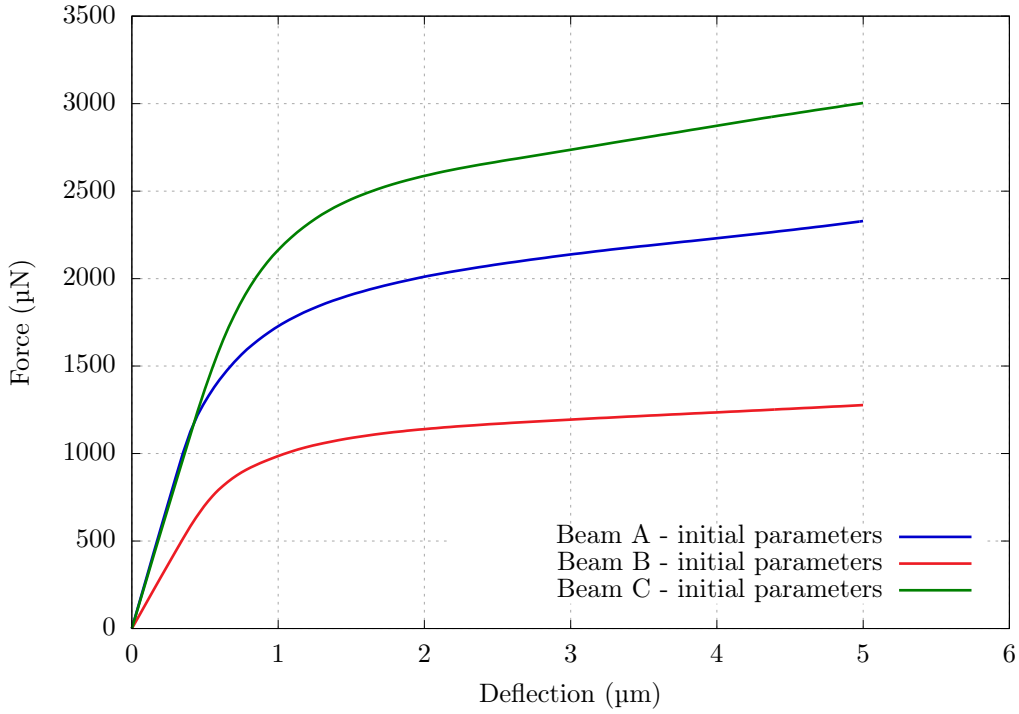

Figure 5.11: Response plots for microbeams A, B and C in Table 5.3 using the Inconel 718 reference parameters in Table 5.1.

obtained are

$$s_6 = 3.135, \quad s_7 = 1.427, \quad s_8 = 0.871, \quad s_9 = 1.109 \tag{5.9}$$

which, if reasonably rounded, correspond to

$$h_\infty = 0.9\,\text{GPa}, \quad h_0 = 8.6\,\text{GPa}, \quad \tau_\infty = 521.2\,\text{MPa}, \quad \tau_0 = 516.3\,\text{MPa}. \tag{5.10}$$

The identified parameter values based on the experimental data are presented in Table 5.4. The corresponding model response using these parameters is plotted together with the experiment data in Figure 5.13.

Table 5.4: Calibrated material parameters for Allvac 718 Plus using data from a single microbeam bending experiment, the one with microbeam B. The values seem inaccurate and are discussed further in Chapter 6.

Allvac 718 Plus (calibrated)										
Elastic parameters			Plastic parameters							
1	2	3	4	5	6	7	8	9	10	11
$C_{11}{}^*$	$C_{12}{}^*$	$C_{44}{}^*$	$\dot{\gamma}_0{}^\dagger$	$m^\dagger$	h_∞	h_0	τ_∞	τ_0	$q_{\alpha\alpha}{}^\dagger$	$q_{\alpha\beta}{}^\dagger$
GPa	GPa	GPa	1/s	–	GPa	GPa	MPa	MPa	–	–
324.5	211.8	154.0	0.10	0.017	0.9	8.6	521.2	516.3	1.0	1.0

*) Value from a non-unique solution, see Subsection 5.3.1.

†) Parameter not subjected to calibration, value for Inconel 718 from Reference [8].

5.3.3 Slip Systems Verification

The experiment beams in Figure 2.3 show clear slip lines. It is interesting to see if the direction of these slip lines can be predicted by slip results from finite element simulations. This can be done by a comparison with developed slip variables γ_1 to γ_{12} for a suitable finite element in the geometry part of interest. A reasonable

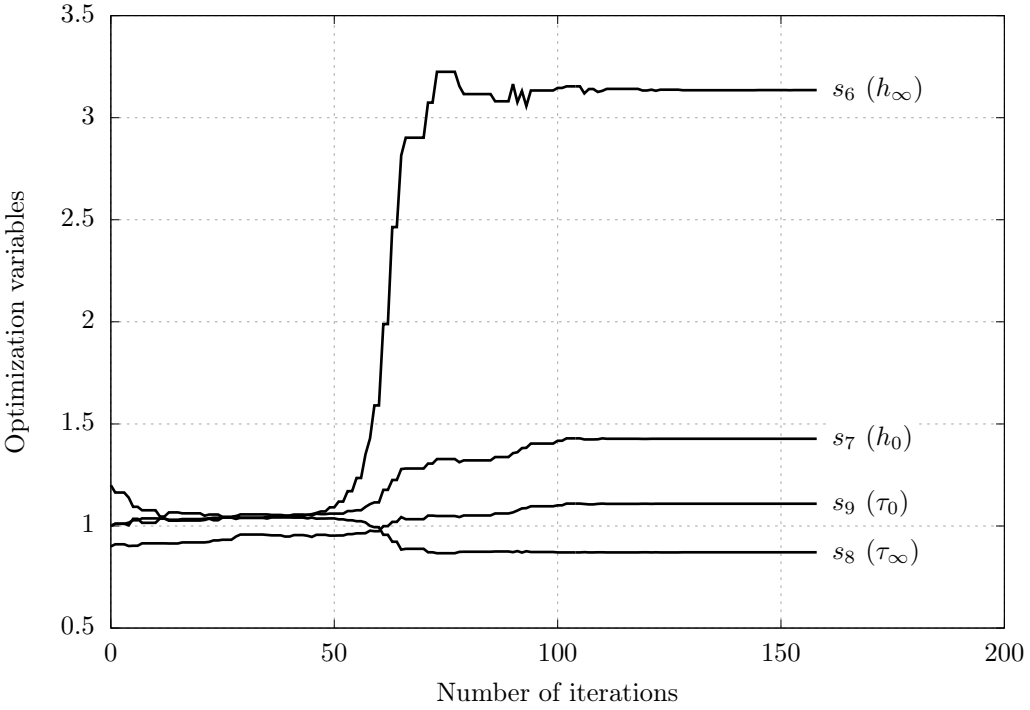

Figure 5.12: Evolution of the optimization variables when calibrating the plastic response to fit the experiment data for microbeam B.

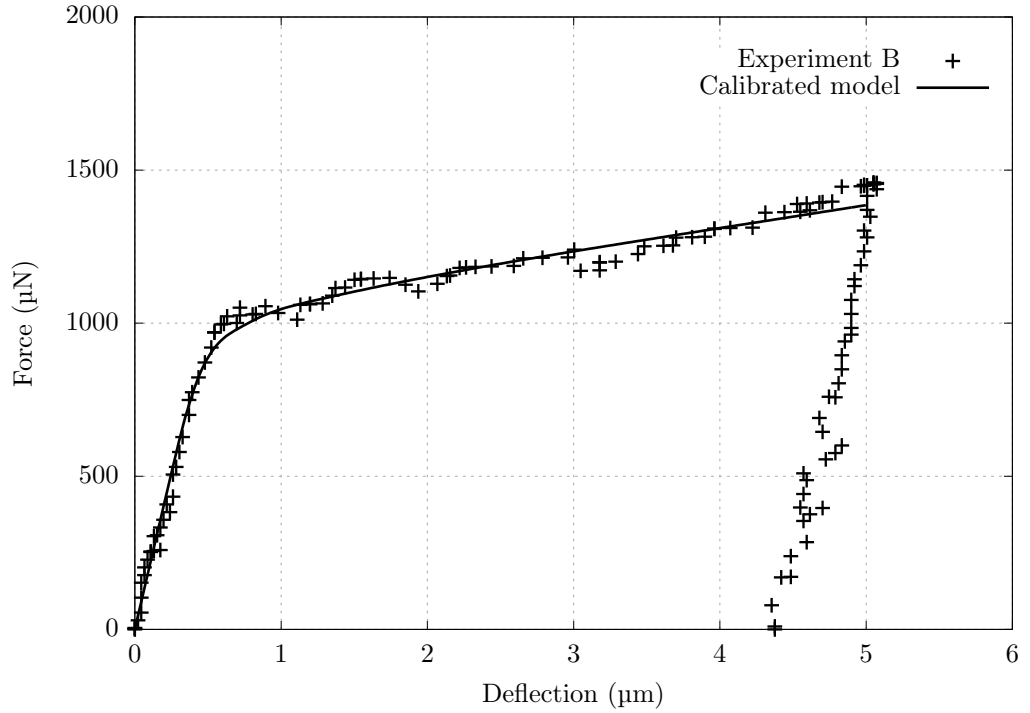

Figure 5.13: Response curves from the experiment with microbeam B and the corresponding finite element model using the calibrated material parameters in Table 5.4.

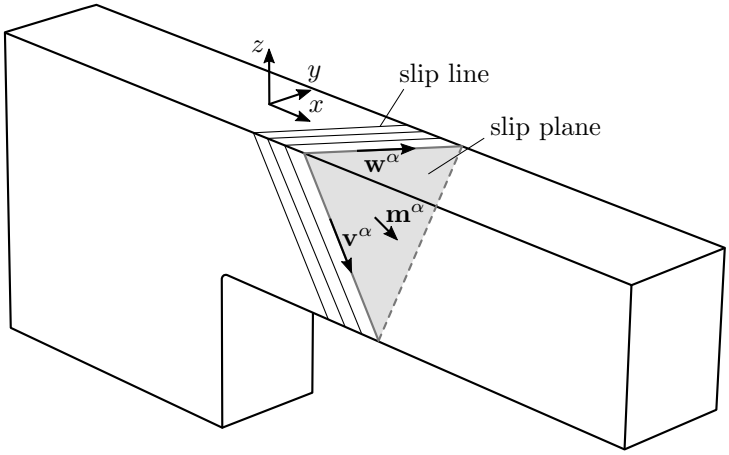

Figure 5.14: Illustration of a slip plane and corresponding vectors used for identifying slip lines.

assumption is that slip lines belong to a slip plane or a linear combination of slip planes. An illustration is given in Figure 5.14.

Consider a vector $\mathbf{v}^\alpha$ as the direction for a line of intersection between the slip plane corresponding to slip system α and any xz-plane. Similarly, let vector $\mathbf{w}^\alpha$ be the direction for a line of intersection between the slip plane corresponding to slip system α and the xy-plane. The slip plane α has the normal vector $\mathbf{m}^\alpha$. These definitions are illustrated in Figure 5.14.

Vectors $\mathbf{v}^\alpha$ and $\mathbf{w}^\alpha$ can be solved for using the equations

$$\mathbf{m}^\alpha \cdot \mathbf{v}^\alpha = m_x^\alpha v_x^\alpha + m_y^\alpha v_y^\alpha + m_z^\alpha v_z^\alpha = 0 \tag{5.11}$$

and

$$\mathbf{m}^\alpha \cdot \mathbf{w}^\alpha = m_x^\alpha w_x^\alpha + m_y^\alpha w_y^\alpha + m_z^\alpha w_z^\alpha = 0. \tag{5.12}$$

Since $v_y = 0$ and $w_z = 0$ by definition, the unit vector solutions are given by

$$\mathbf{v}^\alpha = \begin{cases} \pm\,(0,0,1) & \text{for } m_z = 0, \\ \pm\,(1,0,-m_x/m_z)\,/\sqrt{1^2 + m_x^2/m_z^2} & \text{for } m_z \neq 0 \end{cases} \tag{5.13}$$

and

$$\mathbf{w}^\alpha = \begin{cases} \pm(0,1,0) & \text{for } m_y = 0, \\ \pm(1,-m_x/m_y,0)/\sqrt{1^2 + m_x^2/m_y^2} & \text{for } m_y \neq 0. \end{cases} \tag{5.14}$$

We will now try to verify the slip lines obtained in the experiments for microbeams A, B and C by comparing with the most active slip systems in the simulations. Lines of intersection between the crystal slip planes and the xz-plane are plotted in Figure 5.15a. These may be compared to the slip lines from the experiment SEM images in Figure 5.15b. Estimated slip lines from the images are marked with a red line in both Figure 5.15a and 5.15b. Corresponding plots for the xy-plane are presented in Figure 5.16. Evolution of γ_1 to γ_{12} from simulations with the initial parameters of Table 5.1 are given in Figure 5.17. These slip variables are evaluated for the centroid of the highlighted elements in Figure 5.10.

For the successful experiment with microbeam B, the simulation predicts that system 2 will show most slip followed by system 12, see Figure 5.17. Looking from the xz-view in Figure 5.15, we see that the identified red line falls between the lines representing $\mathbf{v}^2$ and $\mathbf{v}^{12}$. However, looking from above in Figure 5.16, this is not the case.

Slip lines for microbeam A and C may not be representative due to failed experiments. As mentioned in Chapter 2, it looks like these beams have been subjected to significant torsional deformation. In that case, the slip results are most certainly affected. Studying the slip lines for microbeam A and C in the xz-plane (Figure 5.15), the results do not agree with the simulations (Figure 5.17). However, looking at the slip lines from above, i.e. in the xy-plane, the results look better.

The slip system activity from the simulations can not be verified on the basis of Figure 5.15 to 5.17. No conclusions can be made and it is questionable if this analysis method is reasonable.

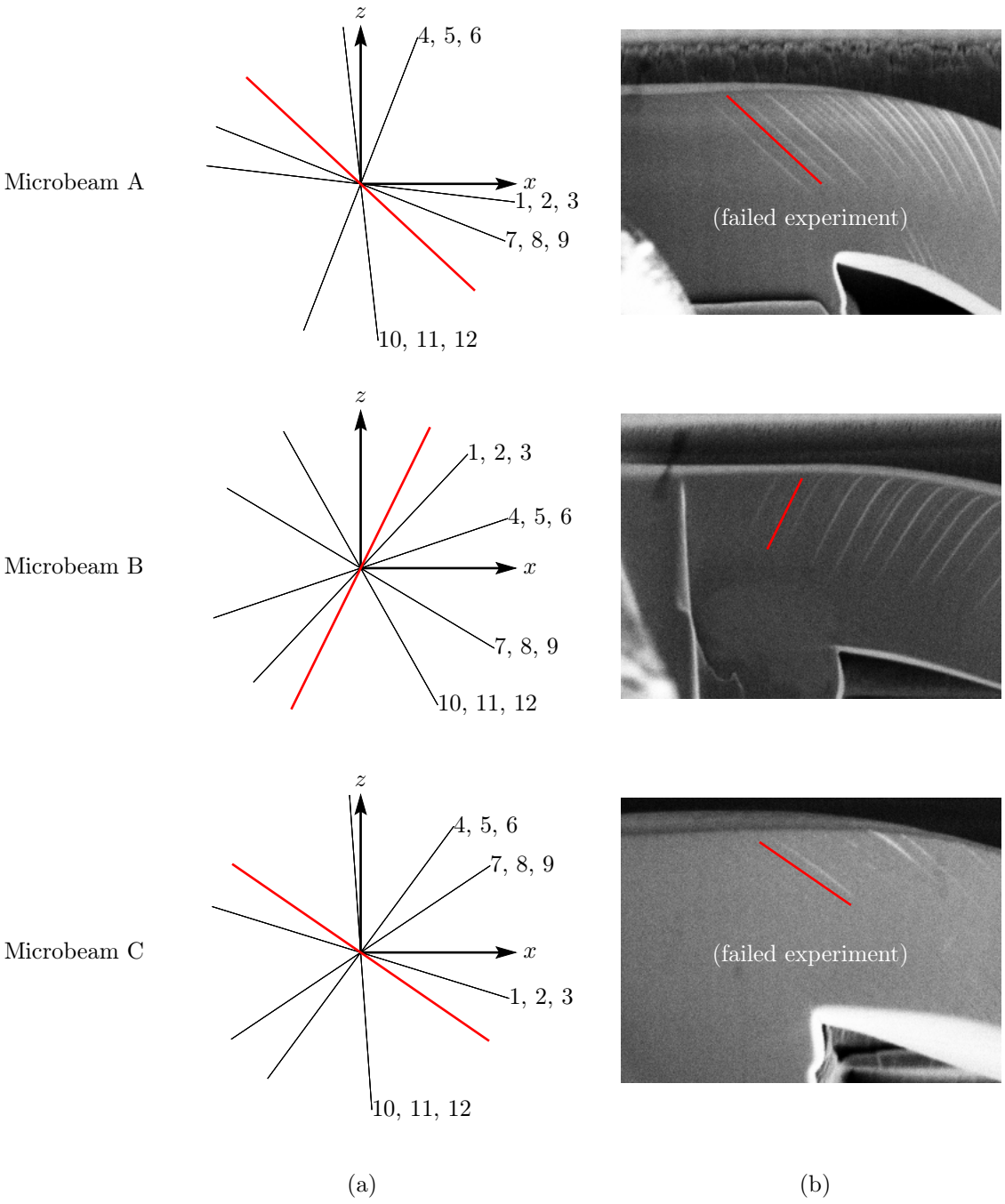

Figure 5.15: (a) Lines of intersection between the initial (before deformation) slip planes and the xz-plane, i.e. vectors $\mathbf{v}^\alpha$. The numbers refer to the slip systems listed in Table 3.1. (b) SEM images from the experiments. Recall that the experiments with microbeams A and C failed.

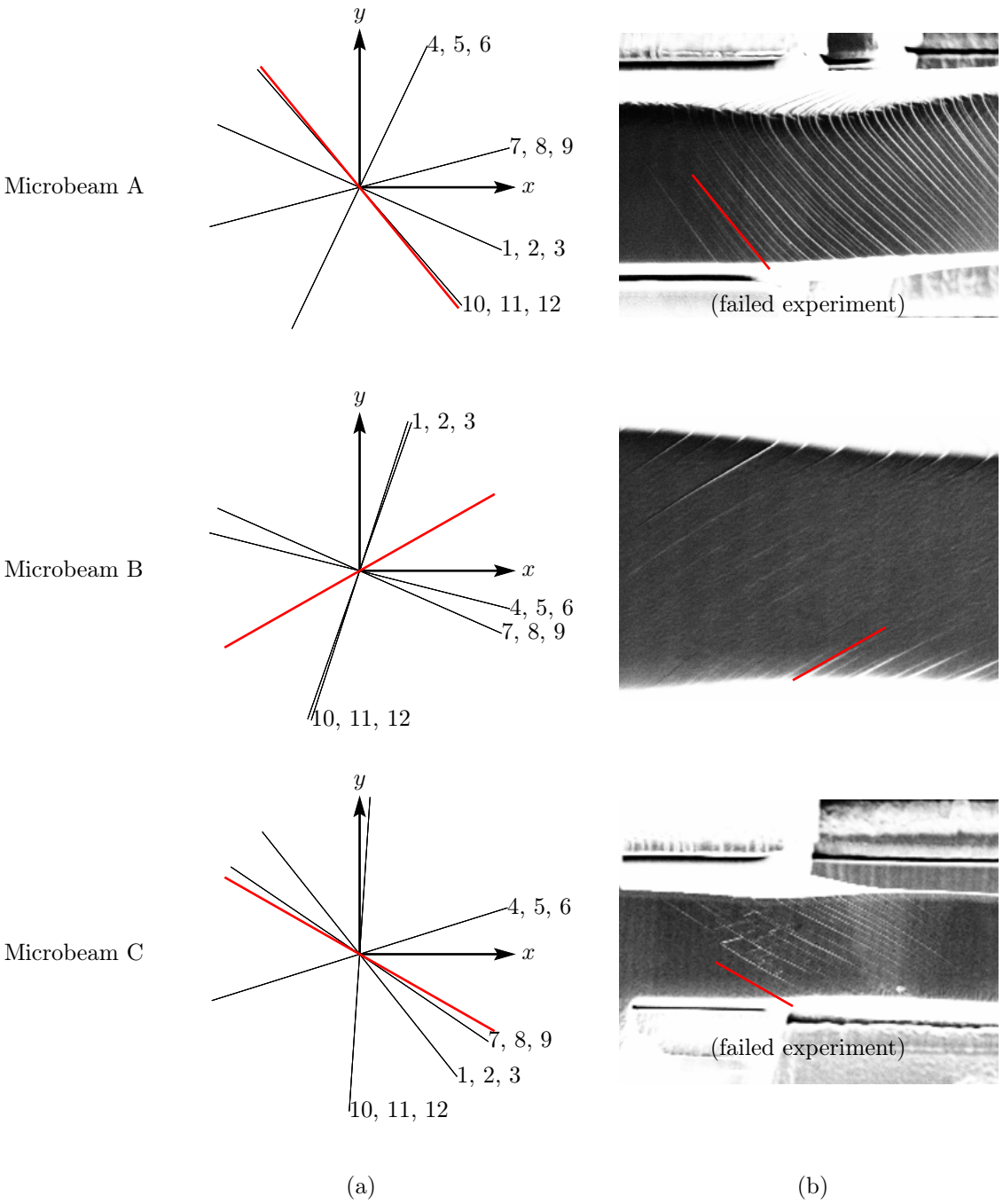

Figure 5.16: (a) Lines of intersection between the initial (before deformation) slip planes and the xy-plane, i.e. vectors $\mathbf{w}^\alpha$. The numbers refer to the slip systems listed in Table 3.1. (b) SEM images from the experiments. Recall that the experiments with microbeams A and C failed.

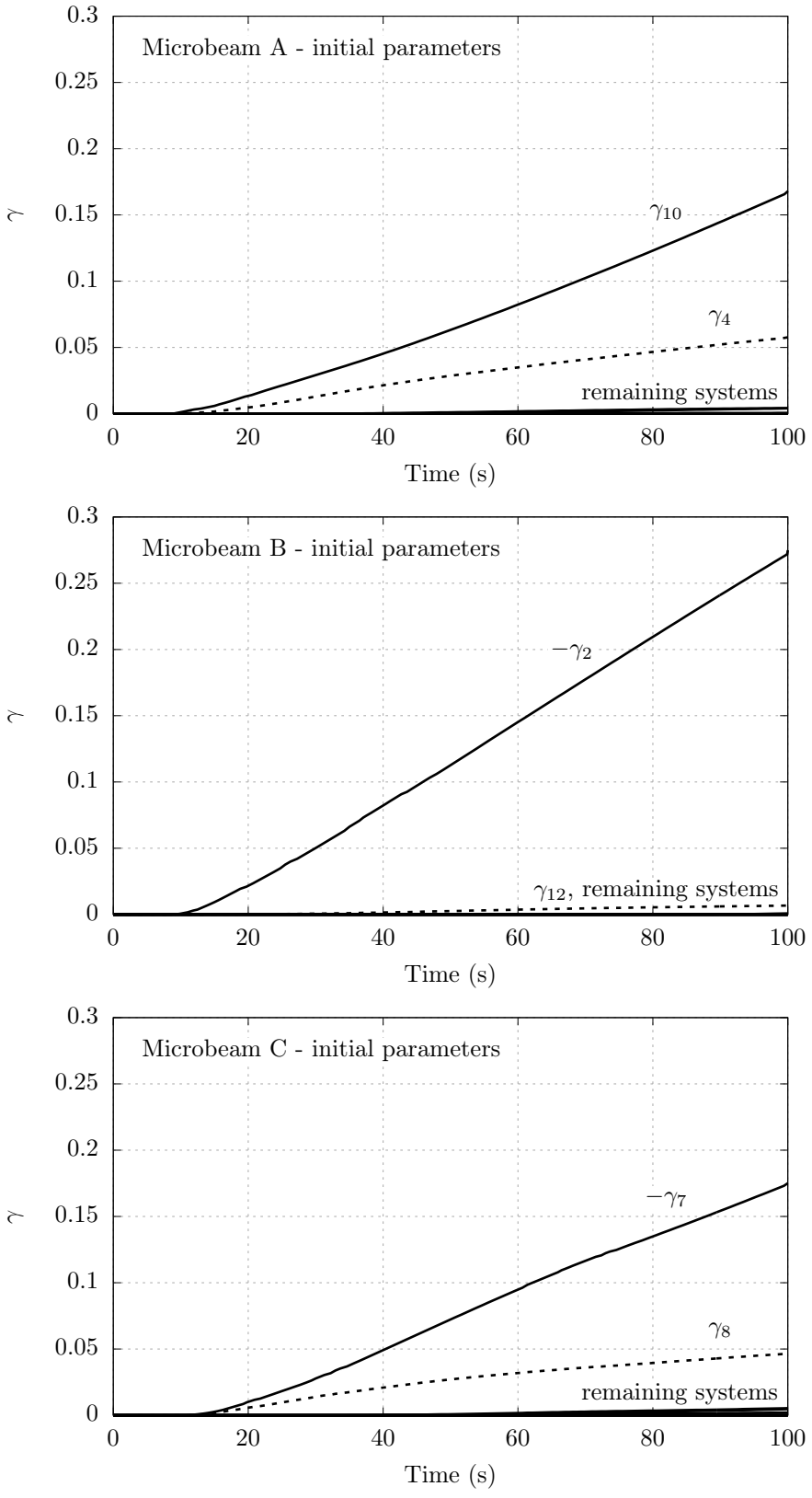

Figure 5.17: Evolution of slip variables γ_1 to γ_{12} for simulations with microbeams A, B and C. The initial material parameters in Table 5.1 are used for the simulations. Slip data is obtained as a centroid average for the highlighted elements in Figure 5.10.

5.4 Boundary Conditions Study

As mentioned in Chapter 4, it is not straight forward what boundary conditions that are most representative for the experiment setup. In Section 5.3 it was observed that the stiffness from the experimental data was much higher than for the finite element model. The boundary conditions may slightly affect this stiffness. We will therefore look at a quick study and compare the force-deflection responses for different boundary conditions.

Some different modeling options with respect to boundary conditions and corresponding responses are shown in Figure 5.18 for microbeam B. The material parameters used are the ones for Inconel 718 in Table 5.1. The black bold lines mark the outlines of the faces that are fixed. Model 1 corresponds to the one used for the calibration. It is seen that the stiffness is barely affected by the model changes. Hence, the discrepancy in stiffness between the model and the experimental data can not be explained by nonrepresentative boundary conditions. Also keep in mind that a refined mesh will lower the force and thereby the stiffness as seen in Chapter 4.

Another interesting observation can be made. Since the force-deflection curves are very similar for all models, we could switch to one of the smaller models to save computational resources. In this case, model 4 seems like a good choice since this response lies closer to the ones of model 1 and 2. However, the simulation times are not affected much since these elements do not yield. In other words, the elements at the back part are computationally cheap.

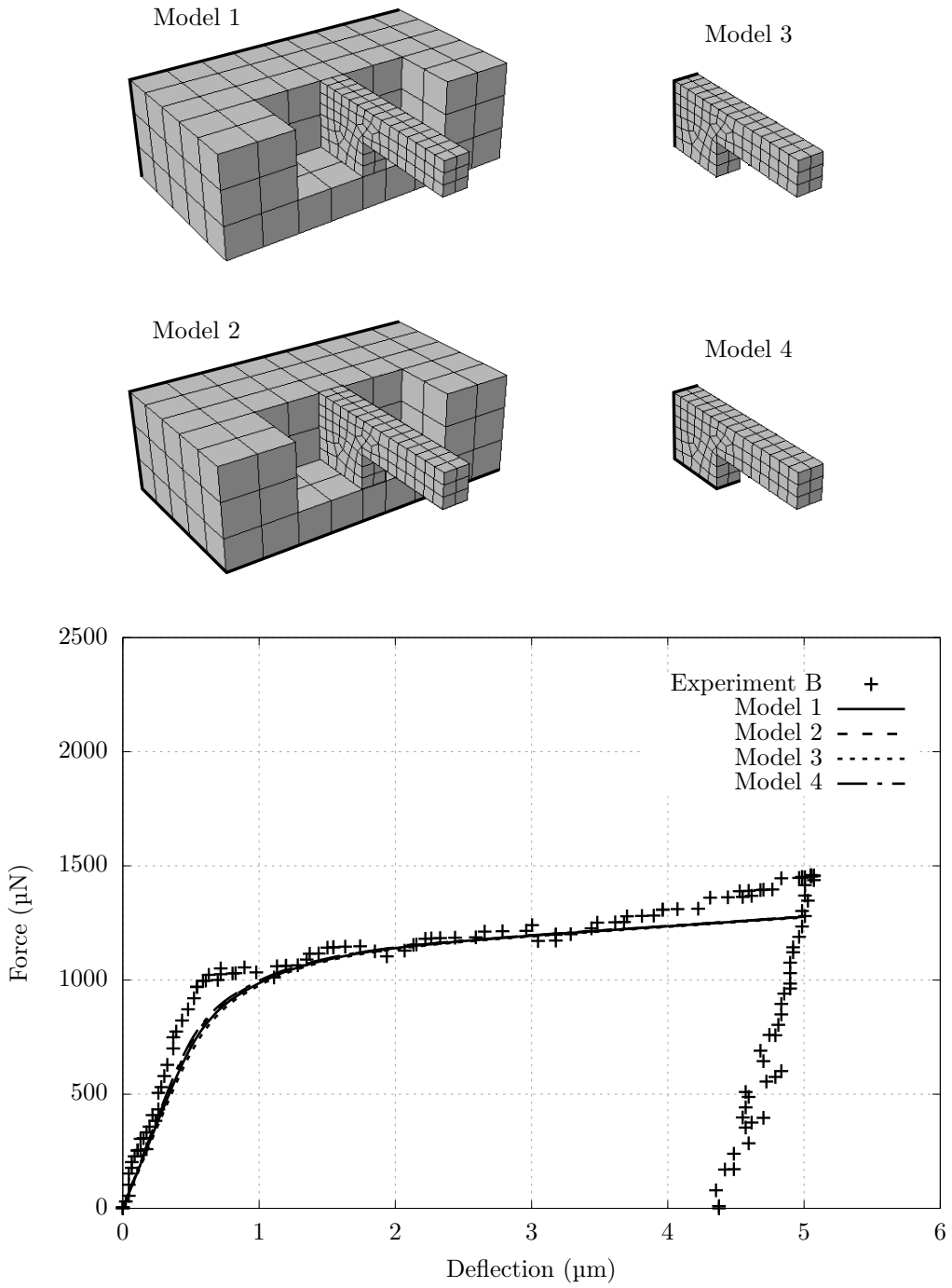

Figure 5.18: Force-deflection plots for microbeam B where experimental data is compared to finite element models with different boundary conditions. Model 1 is fixed only at the back whereas model 2 is fixed at the back and below the structure. In model 3 and 4, only the microbeam part is included in the analysis. Model 3 is fixed at the back and model 4 is fixed at the back and below. All simulations are performed using the Inconel 718 material parameter values in Table 5.1.

6 Concluding Remarks

In this report, the possibility to calibrate a crystal plasticity model using finite element modeling of microbeam bending experiments has been investigated. The microbeam bending experiments are described in Chapter 2. The specimens were prepared and the experiments performed at the Department of Physics at Chalmers by Anand Harihara Subramonia Iyer. Three microbeams were made in total with different dimensions and crystallographic orientation. The microbeams were each milled from a single crystal of the superalloy Allvac 718 Plus. Unfortunately, experimental force-deflection data was only obtained for one of the microbeams since two of the experiments failed.

The crystal plasticity model used in this thesis is introduced in Chapter 3. For simplicity, the crystal plasticity model is presented using small strain theory. A corresponding finite strain theory formulation of the model was used for the simulations in this report. The material user-subroutine for Abaqus was written by Magnus Ekh at the Department of Industrial and Materials Science.

In order to simulate the experiments, a parametrized finite element model of the microbeam structure was developed. The model is generated from a Python script for Abaqus in which the user can specify relevant geometry dimensions, material parameters and analysis settings. Python scripts for postprocessing analysis results, e.g. evaluating force-deflection data, were written as well. More information about the Abaqus Python scripts is available in Appendix A.

Some discussion regarding the modeling is presented in the previous chapters. The influence of fixed boundary conditions for different parts of the microbeam structure was investigated in Section 5.4. We found that the force-deflection response was not significantly affected by switching to other reasonable boundary condition choices. Also, the modeling of the displacement load could be implemented with a contact problem instead of directly prescribing the displacement. However, this would increase the problem complexity and simulation time. One topic that has not been covered is the influence of variations in geometry and the force application. Physical experiments are never perfect and it is good to be aware of parameters that may be extra sensitive to variations.

Next step was to set up an optimization routine to use for the calibration. The interested reader finds details about the calibration programming in Appendix B. In short, a numerical optimization function in Matlab drives the calibration of the material model with underlying Abaqus simulations. The model responses from simulations are compared to experimental data as an objective function. The material model parameters are then updated according to some optimization method, in this case the Nelder-Mead method. New simulations are run and the process continues until some termination criterion is satisfied.

Calibrations of the crystal plasticity model are presented in Chapter 5. Fictitious "experimental data" was first produced by simulations of three different microbeams with same geometry but different crystal orientation. These simulations were performed with a known set of material parameter values. The material parameters were then disturbed and calibrated to fit the fictitious "experimental data". Regarding the elastic response (governed by the parameters C_{11}, C_{12} and C_{44}), we found that the solution was (or at least very close to) non-unique. More response information is needed in order to accurately find all three elastic parameters, force-deflection curves are not enough. It is suggested that multiaxial response information could be the solution, analogously to measuring the transverse deformation when determining Poisson's ratio for an isotropically linear elastic material. No attempt was made to include an additional response measure in the calibration process.

The plastic parameters were then calibrated for the fictitious data in Subsection 5.2.2. To limit the calibration problem, only four out of eight plastic parameters were considered: h_∞, h_0, τ_∞ and τ_0. We observed in the calibration that the sensitivities w.r.t. force-deflection curves seem to be higher for τ_∞ and τ_0 when compared to h_∞ and h_0. Parameters τ_∞ and τ_0 found relatively quickly their way back to the original values, see Figure 5.6. Anyway, the fictitious plastic calibration problem with regards to only these four parameters seems to be well-defined.

Parameters $\dot{\gamma}_0$, m, $q_{\alpha\alpha}$ and $q_{\alpha\beta}$ were not calibrated for different reasons. We realized in the parametric study in Subsection 5.2.3 that parameters $q_{\alpha\alpha}$ and $q_{\alpha\beta}$ could influence the force-deflection curves in a similar way as the parameters that were calibrated. This could lead to another problem with a non-unique solution and this is part of the reason why some parameters were omitted from the calibration. However, this could potentially be a serious issue worth looking further into in future work. When slip in multiple slip systems are active, one can argue that it must be important to use accurate values for $q_{\alpha\alpha}$ and $q_{\alpha\beta}$.

In Section 5.3, we looked into a calibration of the material parameters using data from the successful real microbeam bending experiment. As for the elastic calibration of the fictitious "experimental data", no unique solution for the elastic parameters could be found. However, the elastic response in the experimental data

(Allvac 718 Plus material) was much stiffer than the one predicted from the simulation with the Inconel 718 parameter values. Since the elastic parameters of Inconel 718 and Allvac 718 Plus can be expected to be similar, something seems to be incorrect. We also examined and concluded in Section 5.4, that changing to other, possibly more suited, boundary conditions do not increase the elastic microbeam stiffness much. The experimental data may not be accurate enough to calibrate the elastic parameters. Anyway, two constraints were needed in order to specify values of C_{11}, C_{12} and C_{44}. As expected, the values of the calibrated elastic parameters turned out to be unrealistically high. We concluded that it may not be reasonable to accurately calibrate the elastic parameters from the currently available microbeam bending experiment. More samples could be used to confirm this and rule out other error sources.

The plastic parameters h_∞, h_0, τ_∞ and τ_0 were then calibrated based on the experimental data. The final calibrated response in Figure 5.13 seems to be the best fit that this crystal plasticity model can achieve. In that regard, the calibration was successful. Values for the more sensitive parameters τ_∞ and τ_0 were rather close to the Inconel 718 numbers in Table 5.1. However, the hardening parameter h_∞ was significantly increased to fit the experimental data. To be able make any further conclusions we would need to have more experimental data to work with.

The specimens show characteristic slip lines after yielding. The slip lines from SEM images of the experiment microbeams were compared with the active slip systems in Subsection 5.3.3. No verification or major conclusions could be made which is a bit worrying. Errors in the analysis or EBSD measurements should not be ruled out as possible explanations. It could also be the case that slip lines are not representative of the most active slip systems when multiple systems show significant slip.

It should be noted that rather coarse meshes were used throughout all the calibration in the previous chapter. This was a decision based on not only computational resources, but also limitations in Abaqus. When performing numerical optimization tasks very many simulations are needed. Using an implicit finite element formulation, the scaling obtained with multiple CPU:s or cores is not particularly good. We would of course prefer results obtained with a finer mesh where it is possible to show fully converged model responses.

There are other issues or error sources not yet mentioned. Statistical scatter is always present when dealing with experiments and these variations are likely more pronounced on the microscale as compared to the macroscale. The crystal orientations may also not be constant over the whole microbeam which could affect both the calibration and the slip lines validation.

6.1 Suggestions for Future Work

In future work it is of course desired to have more experimental data to study. Not only can we expect more accurately calibrated parameters, more samples could give an insight into the experimental data accuracy as well. It would also be helpful to have reference experiments with the same setup using another material, e.g. Inconel 718 in this case. It is then preferred to have similar orientations and geometry when comparing materials to clearly be able to link differences in the force-deflection response to the material. I would also recommend to look into if there are alternatives to the current "spring table" experiment setup to obtain a more accurate force-deflection data.

The elastic parameters will be hard to accurately calibrate using microbeam bending experiments. First and foremost, calibration of elastic parameters requires very good data accuracy for small elastic deflection ranges. The data accuracy with the current "spring table" seems to be insufficient. Secondly, the calibration results show that more response information is required to determine the elastic parameters. A multiaxial response for the microbeam bending would in practice require SEM images from multiple views at the same time. There may be other types experiments, like tensile bar experiments, which are more suitable for the purpose of calibrating the elastic parameters. For a bar problem, it could be possible to capture both elongation and transverse deformation from a single view. An SEM image of microbeam B from a top-view after the experiment is given in Figure 6.1 to illustrate the transverse deformation idea.

If the experimental data accuracy can not be improved for the microbeam bending experiments, I would simply skip the elastic parameters and only focus on the plastic ones. When the calibration of the plastic parameters is performed, one could then choose to only look at the plastic part of the deflection and adjust the data and model response accordingly.

On the modeling issue with the coarse discretization, it is hard to see a more refined mesh for calibration jobs. However, one could think of a setup where a first "rough" calibration is performed with a coarser mesh. The calibrated variables may then be used as an initial guess for a calibration with a finer mesh. Regarding

Microbeam B
top-view

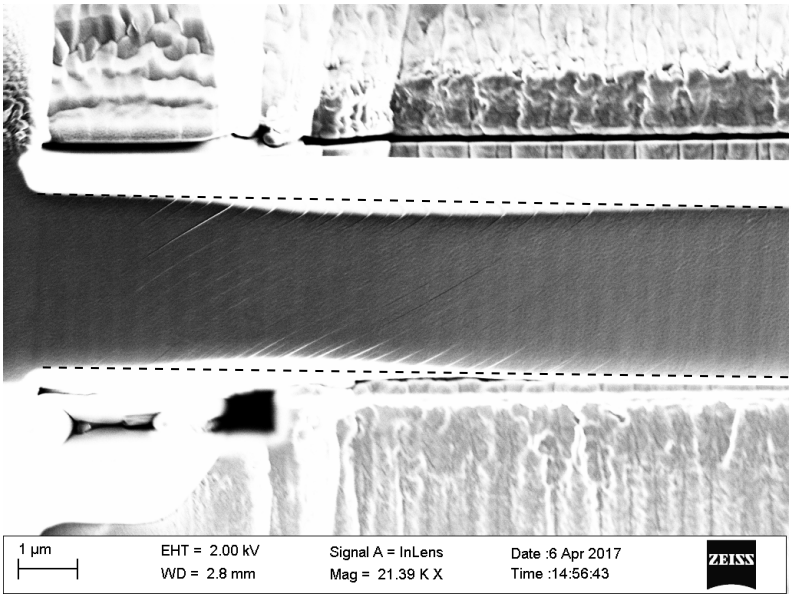

Figure 6.1: SEM image from a top-view (xy-view) of microbeam B after the experiment. Significant contraction (from a tensile deformation) of the upper part of the microbeam is noted.

the modeling of the force application with the diamond tip, it would be interesting to compare the results of a prescribed boundary to a contact problem implementation. I expect similar results due to Saint-Venant's principle, but it could be an exercise to perform for completeness.

References

[1] M. C. Kushan et al. Allvac 718 Plus Superalloy for Aircraft Engine Applications. *Recent Advances in Aircraft Technology, Edited by Dr. Ramesh Agarwal* (2012).

[2] D. Di Maio and S. G. Roberts. Measuring Fracture Toughness of Coatings Using Focused-ion-beam-machined Microbeams (2004).

[3] O. Kraft, R. Schwaiger, and W. D. Nix. Measurement of Mechanical Properties in Small Dimensions by Microbeam Deflection (1998).

[4] F. Roters et al. Overview of Constitutive Laws, Kinematics, Homogenization and Multiscale Methods in Crystal Plasticity Finite Element Modeling: Theory, Experiments, Applications. *Acta Materialia* **58** (2010), 1152–1211.

[5] *Euler Angles*. `https://en.wikipedia.org/wiki/Euler_angles`. Accessed: 2017-06-13.

[6] F. Birch. Finite Elastic Strain of Cubic Crystals (1947).

[7] G. Martin et al. A Multiscale Model for the Elastoviscoplastic Behavior of Directionally Solidified Alloys: Application to FE Structural Computations. *International Journal of Solids and Structures* **51** (2014), 1175–1187.

[8] A. Cruzado et al. Multiscale Modeling of the Mechanical Behavior of IN718 Superalloy Based on Micropillar Compression and Computational Homogenization. *Acta Materialia* **98** (2015).

[9] Abaqus. *Abaqus 6.13 Documentation*. 2013.

[10] E. Q. Sun. *Shear Locking and Hourglassing in MSC Nastran, ABAQUS, and ANSYS*. `http://web.mscsoftware.com/events/vpd2006/na/presentations/tech_papers/27.pdf`. Accessed: 2017-05-30.

[11] M. Ekh, R. Lillbacka, and K. Runesson. A Model Framework for Anisotropic Damage Coupled to Crystal (visco)Plasticity. *International Journal of Plasticity* **20** (2004), 2143–2159.

[12] *Zener Ratio*. `https://en.wikipedia.org/wiki/Zener_ratio`. Accessed: 2017-05-15.

A Abaqus Python Scripting

The Abaqus software provides interfaces via its own Python language, usually called "Abaqus Python" or "Python for Abaqus", or C++. It is possible to run scripts directly from a terminal, but Abaqus also has a command line interface (CLI) for the interactive Abaqus Python mode in its graphical user interface (GUI). In fact, all model actions performed in the GUI have an equivalent Python statement or block of statements. There is a "macro recorder" in the Abaqus GUI which produces Python scripts that can be of great help when writing own scripts.

Scripting for Abaqus, either using Python or C++, provides good opportunities to automate repetitive tasks. It is also possible to perform tasks that are not possible or very complicated directly in the GUI, like advanced postprocessing for instance. Two Abaqus Python scripts have been written for the microbeam bending analysis. The first script uses Abaqus to set up a model and produce a corresponding input file. The second script performs a postprocessing job on an output database from an analysis.

A.1 Model Setup Script

The model setup script produces a microbeam model from scratch taking various parameters into account. The following work flow has been adopted in the script:

1. *Definition of parameters.* These parameters are used for geometry, materials, mesh, load steps and time incrementation.
2. *Setup of materials.* The crystal plasticity material model is defined from material parameters. The oxide layer also needs a material model, if one is to be included.
3. *Sketching of geometry.* Sketches are made from which the part geometry is created in the next step.
4. *Creation of parts.* Due to the simple microbeam geometry, it can be created by multiple extrusions together with a built-in function for creation of the fillet under the beam. Multiple parts may be created. This is the case if an oxide layer is to be included with another material model.
5. *Creation of instances.*
6. *Meshing of instances.*
7. *Creation of steps and boundary conditions.*
8. *Setup of job.*

A.2 Postprocessing Script

A script is also written to postprocess the analysis results and write relevant data to an output file. Information is written with total time, step time, beam tip deflection and edge reaction force for each time increment.

In Abaqus, a step is an object used to conveniently split up an analysis in natural sequences. These sequences are typically defined by changes in loads, boundary conditions or interactions. Note that what is often called a "time step" in nonlinear finite element literature is in Abaqus referred to as a time increment, which in turn belongs to an Abaqus step.

B Calibration Programming

This appendix chapter describes how a numerical optimization task may be performed using underlying Abaqus simulations. The methods described here are used to calibrate the crystal plasticity model in this thesis.

Calibration of the parameters in the crystal plasticity model is performed according to Figure B.1. Since the Abaqus software lacks a sophisticated calibration module for material model parameters, an external optimization code is used instead. This is preferably done using a high-level language suitable for scientific calculations like Matlab or Python. In this case, Matlab is used. The Nelder-Mead method (also called the Simplex method) is used which is implemented in Matlabs function `fminsearch`, see Figure B.1.

The first step is to produce an Abaqus input file (text file) for the finite element model. As described in Appendix A, an Abaqus Python script is written to set up the model and produce an input file. Most information in the input file will remain constant throughout the calibration process.

Next step is to write a function which is passed on as a function handle to `fminsearch`. This function takes the variable material parameters (optimization variables) as input arguments and returns an objective function value, see Figure B.1. The operations of this function may be summarized as:

1. **Overwrite the Abaqus input file with the new optimization variables**. As an example, the lines defining an isotropic linear elastic material may be given by:

   ```
   *Material, name=Material-Oxide
   *Elastic
   275000.0, 0.25
   ```

   A straightforward approach is to read all the text file lines and find the one that starts with the string `'*Material, name=Material-Steel'`. With the index of this line known, one can then replace the line with the parameters two lines below and overwrite the file.

2. **Perform an Abaqus job call with the new input file**. This can be done in Matlab using the function `system`, which is used to execute operating system commands:

   ```
   system('abaqus job=Job-Microbeam')
   ```

3. **Wait for the job to be completed**. Abaqus writes an output database file with extension `.odb` containing model information and analysis results. While Abaqus has this output database file open with write access, a database lock file with extension `.lck` is present in the working directory. Therefore, before accessing the output database, we need to wait until the lock file is no longer present. A Matlab function is written for this purpose. The lock file also remains in the folder if errors are encountered during the analysis.

4. **Run an Abaqus Python script which postprocesses the output database results**. The results of interest are then written to an output text file.

   ```
   system('abaqus viewer noGUI=microbeam_postprocess.py')
   ```

5. **Wait for the postprocess to be completed**. See step 3.

6. **Read the output data text file produced in the previous step**.

7. **Evaluate the objective function value which is then returned**.

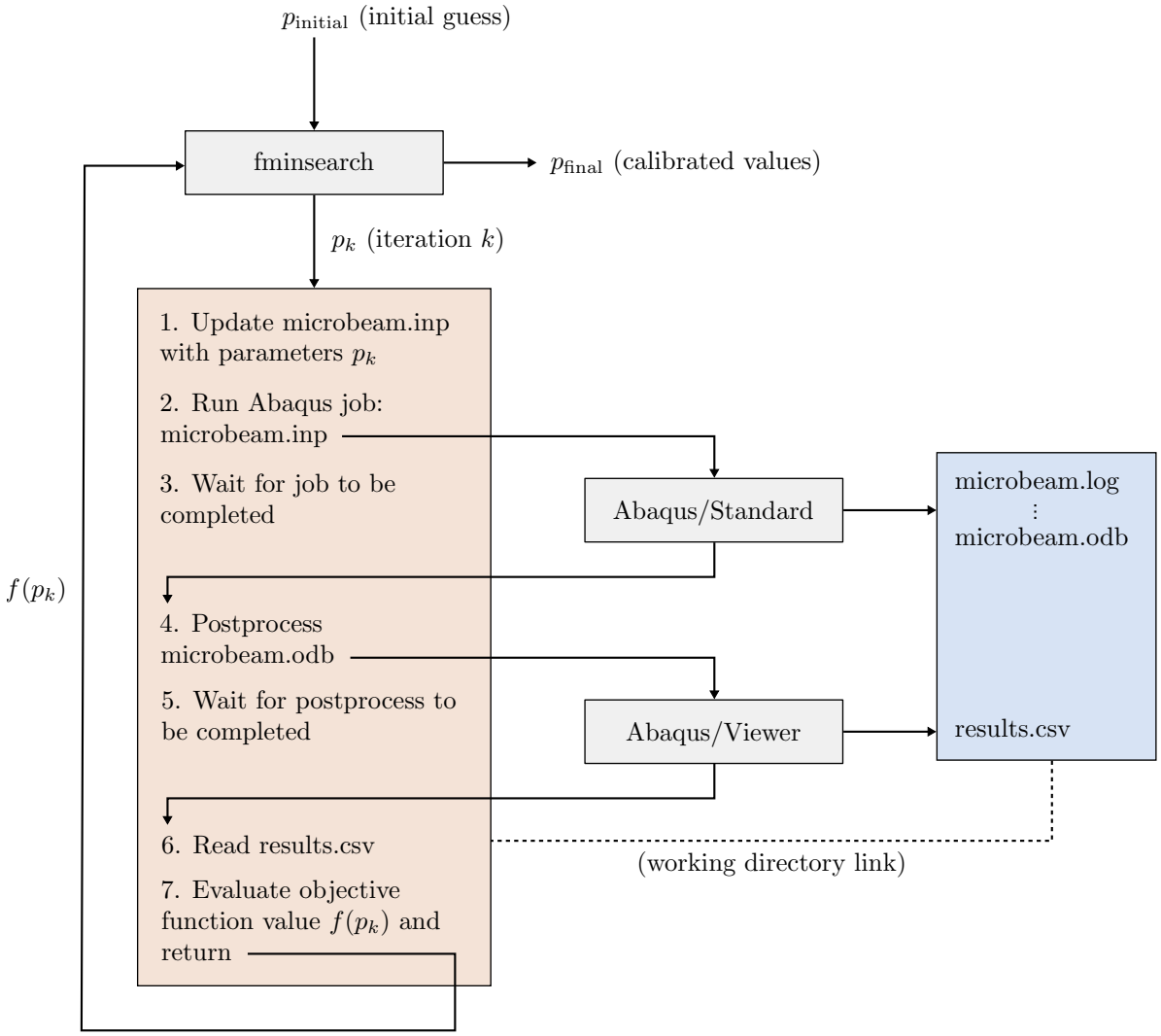

Figure B.1: Illustration of how the material parameters can be calibrated using optimization code in Matlab with underlying Abaqus simulations.